Geophysical Journal International

Geophys. J. Int. (2023) **232,** 615–642
Advance Access publication 2022 September 6
GJI Marine geosciences and applied geophysics

https://doi.org/10.1093/gji/ggac350

Three-dimensional *S*-wave velocity structure of oceanic core complexes at 13°N on the Mid-Atlantic Ridge

C. Peirce [1], M.J. Funnell [1], T.J. Reston[2] and C.J. MacLeod [3]

[1] *Department of Earth Sciences, Durham University, South Road, Durham DH13LE, UK. E-mail: christine.peirce@durham.ac.uk*
[2] *School of Geography, Earth and Environmental Sciences, University of Birmingham, Edgbaston, Birmingham B152TT, UK*
[3] *School of Earth and Ocean Sciences, Cardiff University, Park Place, Cardiff CF103AT, UK*

Accepted 2022 September 1. Received 2022 August 25; in original form 2022 May 3

SUMMARY

13°N on the Mid-Atlantic Ridge is regarded as a type site for oceanic core complexes (OCCs). Within ∼70 km along the spreading centre, it hosts four OCCs in different stages of their life cycle making this an ideal location to determine how OCCs are formed, and what drives the hydrothermal circulation that sustains the vent fields associated with them. Here we describe the results of *S*-wave seismic tomographic modelling within a 60 × 60 km footprint containing several OCCs, the spreading centre and both flanks. A grid of 17 wide-angle seismic refraction profiles was shot within this footprint and recorded by a network of 46 ocean-bottom seismographs (OBS). Approximately 6200 *S*-wave arrival travel times have been modelled, constraining primarily the velocity–depth structure of the upper-to-mid crust. Depth slices through the resulting 3-D *S*-wave velocity (*Vs*) model reveal the OCCs located at 13°20′N and 13°30′N to each have a region of relatively low *Vs* (<3 km s^{-1}) beneath its detachment, and a higher *Vs* (>3 km s^{-1}) in the inter-OCC basin and regions surrounding the detachments. Using the equivalent 3-D *P*-wave velocity (*Vp*) model of Simão *et al.* (2020), the corresponding *Vp*/*Vs* model is calculated to investigate lithology, permeability and the existence of any off-axis magmatic intrusions that may drive fluid flow. The *Vp*/*Vs* model clearly shows that the crust beneath the deep lava-floored inter-OCC basin is characteristically oceanic (*Vp*/*Vs* ratio of <1.85) in velocity–depth structure, in contrast to the OCCs themselves which have a *Vp*/*Vs* ratio of >1.85, suggesting that they formed under magma poor (tectonic) conditions. The *Vp*/*Vs* model also shows that the OCCs are not connected, at least to mid-crustal level. Alternatively, if the OCCs lie on the same detachment surface, that surface would have to undulate >3km in amplitude over a distance of <20 km for these OCCs to appear to be unconnected. Our 3-D *S*-wave and *Vp*/*Vs* models thus support MacLeod *et al.*'s (2009) model of localized OCC evolution. Our *S*-wave velocity model also suggests that the Irinovskoe (13°20′N) and Semyenov (13°30′N) vent fields have different hydrothermal circulation drivers, with the Semyenov field being driven by magma intrusion(s) and the Irinovskoe field being driven by the spreading centre thermal gradient and pervasive flow along open permeability within the detachment footwall, perhaps further opened by roll-over to lower dip angle as it exhumes at the seabed.

Key words: Controlled source seismology; Crustal imaging; Crustal structure; Mid-ocean ridge processes.

1 INTRODUCTION

Globally, new oceanic crust forms at mid-ocean ridges over a range of spreading rates up to 150 mm yr^{-1}. This broad range in spreading rate results in a diversity of mechanisms by which the crust forms, that are typically dominated by magmatic input at faster spreading rates and increasingly accommodated by tectonic (magma poor) spreading at slower spreading rates (Dick *et al.* 2003; Buck *et al.* 2005). At the slowest spreading rates, where magmatic activity is absent or negligible over 10 s of kilometres along axis, and for 100 s of thousands of years, long-lived detachment faults (Cann *et al.* 1997; Tucholke *et al.* 1998) accommodate the majority of the extension

on one side of the spreading centre, resulting in highly asymmetric seafloor separation, morphology and lithology (MacLeod *et al.* 2009; Mallows & Searle 2012).

Various mechanisms have been proposed to explain the evolution of such detachment faults, with most related to the magmatic fraction of formation, M (Buck *et al.* 2005). M is a simple scale of whether magmatic dykes account for all of the plate separation ($M = 1$) or none of it ($M = 0$), with faults moving away from the spreading axis when $M > 0.5$, and remaining stationary when $M = 0.5$. Fundamentally, M controls the rate of fault migration off-axis, and so, when M is high, faults readily migrate from the ridge axis and cool quickly, making slip on them less favourable and encouraging the formation of new faults. When M is low, faults migrate slower and remain active for longer (Buck *et al.* 2005; Howell *et al.* 2019).

Thus, based on the magmatic fraction of formation, detachment surfaces form and remain stable when $M = 0.5$ (Buck *et al.* 2005), and then relatively small changes in the magmatic state of the ridge axis control whether slip does or does not occur along them at any point in time. Through their initiation and evolution, detachment faults enable the exhumation of deep crustal and upper mantle rocks to the seabed, and have seismicity patterns that characterize their mechanism of formation and subsequent deformation. Originally, it was proposed that the initial steep footwall rotates to a low angle as the crust migrates from the ridge axis, placing it under tension (Buck 1988; MacLeod *et al.* 2002; Escartín *et al.* 2017; Howell *et al.* 2019) and resulting in the formation of high-angle faults throughout the detachment surface (Tucholke *et al.* 1998; Blackman *et al.* 2008, 2009). More recently, it has been suggested, instead, that the detachment fault surface is naturally curved and under neutral stress conditions, and moves by block rotation 'unbending' with increasing distance from the spreading axis (Sandiford *et al.* 2021). A fundamental contradiction between these mechanisms is that the flexural model invokes compression deep within the footwall (Buck *et al.* 2005; Howell *et al.* 2019) as supported by seismological observations at the 13°20'N Mid-Atlantic Ridge (MAR) detachment fault (Parnell-Turner *et al.* 2017), whereas the block rotation model places this region under tension (Sandiford *et al.* 2021), and equates shortening strain rates to seismicity using observations at the Trans-Atlantic Geotraverse (TAG) detachment (deMartin *et al.* 2007).

The along axis extent of detachment faulting continues to be debated, and focuses on whether they are local- (e.g. MacLeod *et al.* 2009) or segment-scale (e.g. Smith *et al.* 2006, 2008) features. The segment-scale model requires a single long-lived detachment surface to be continuous along axis (Smith *et al.* 2008) and have portions that may be covered by rafted blocks of more typical axial lavas and rubble (Reston & Ranero 2011). Conversely, the local-scale model (MacLeod *et al.* 2009) distinguishes between independent detachment surfaces that are controlled by lateral and temporal variations in magma supply. This model is supported by geophysical evidence comprising adjacent seismically distinct volumes of crust and upper mantle material (e.g. Peirce *et al.* 2019a, 2020; Simão *et al.* 2020), and unconnected fault planes delineated by microseismicity (e.g. Parnell-Turner *et al.* 2017, 2021).

Exhumed detachment surfaces, or oceanic core complexes (OCCs), are thus the footwall of an extensional fault, and are often bound on the spreading centre-distal side by a series of ridges and seafloor of chaotic morphology, with exposed sections of mafic rocks representing the initial breakaway of the detachment (Cannat 1993; Blackman *et al.* 1998; MacLeod *et al.* 2009). They asymmetrically accommodate the majority of plate separation, and significantly influence spreading ridge morphology (e.g. Escartín *et al.* 2008; Smith *et al.* 2008; Schouten *et al.* 2010; Grevemeyer *et al.* 2013). The OCC itself is typically defined by an extensive convex-up surface that has ridge-perpendicular striations (e.g. MacLeod *et al.* 2009; Searle *et al.* 2019), and comprises a combination of mantle and gabbro lithologies (e.g. Tucholke & Lin 1994; Cann *et al.* 1997; Tucholke *et al.* 1998; Escartín & Canales 2011; Sauter *et al.* 2013) that are likely interspersed (Reston *et al.* 2002; Reston & Ranero 2011; Harding *et al.* 2017). As OCCs evolve and migrate away from the spreading centre, they either become increasingly intruded by gabbro or dissected by the adjacent spreading centre (Parnell-Turner *et al.* 2017; Reston 2018). Dredging and drilling have sampled rocks that are highly altered, and many OCCs host hot- or cold-smoker hydrothermal vent systems, that demonstrate active fluid circulation through them.

The surface expression of the detachment terminates at a 'moat' that demarcates the onset of an apron of hummocky volcanic and sedimented material (Searle *et al.* 2019). The lateral extent of the apron and the extent of its coverage of the OCC, depends on the dip angle of the detachment surface, with lower angles (<13°; e.g. TAG–Canales *et al.* 2007) promoting the covering of the surface, compared to higher angles (>13°; e.g. 13°20′N MAR) where friction is overcome and sediments instead accumulate in the basal apron (Olive *et al.* 2019).

Investigation of OCC structure has typically been undertaken through lithological sampling (e.g. Escartín *et al.* 1997, 2003a; Dick *et al.* 2000; Blackman *et al.* 2002, 2006, 2019; Fujiwara *et al.* 2003; Kelemen *et al.* 2004; Ildefonse *et al.* 2007; MacLeod *et al.* 2009; Bonnemains *et al.* 2017) and imaging by shipboard (e.g. MacLeod *et al.* 2009) and towed systems (e.g. Reston *et al.* 2002; Canales *et al.* 2004, 2008; Collins *et al.* 2009; Grevemeyer *et al.* 2018b; Peirce *et al.* 2019a, 2020), or submersible vehicles (e.g. Searle *et al.* 2019). Seismic imaging provides kilometre-scale subseabed structure, enabling changes in crustal thickness (e.g. Reston *et al.* 2002), variations in internal velocity structure relative to background oceanic crust (e.g. Blackman *et al.* 2009; Peirce *et al.* 2019a, 2020; Simão *et al.* 2020) and likely lithological composition (Harding *et al.* 2017; Grevemeyer *et al.* 2018b; Peirce *et al.* 2020) to be determined. Despite the increasing wealth of seismic data, the recording of high-quality data from ocean-bottom seismographs (OBSs) deployed at such sites remains challenging, as the highly variable seabed morphology and limited sediment cover promote seismic scattering and reduce coupling between the seabed and instrument (e.g. Collier & Singh 1998; Peirce *et al.* 2019a, b, 2020).

The 13°N segment of the MAR (Fig. 1) hosts a number of OCCs that have been studied using bathymetry and dredging campaigns (e.g. MacLeod *et al.* 2009; Bonnemains *et al.* 2017), as well as larger-scale passive hydrophone array seismicity experiments (Smith *et al.* 2003; Escartín *et al.* 2003b). To investigate variation in subsurface structure and accretionary processes along the 13°N spreading centre, three research expeditions were undertaken on the RRS James Cook that focussed on the formation and evolution of adjacent OCCs: JC102 (Peirce 2014a), JC109 (Peirce 2014b) and JC132 (Reston & Peirce 2016). Together, these expeditions undertook a range of active and passive geophysical data acquisition, including:

(i) Local microseismicity by passive OBS deployment (Parnell-Turner *et al.* 2017), as well as during hiatuses in the shooting phase of the active-source OBS deployment (Parnell-Turner *et al.* 2021), to resolve spatially and temporally variable patterns that reveal the active movement and evolution of adjacent OCCs.

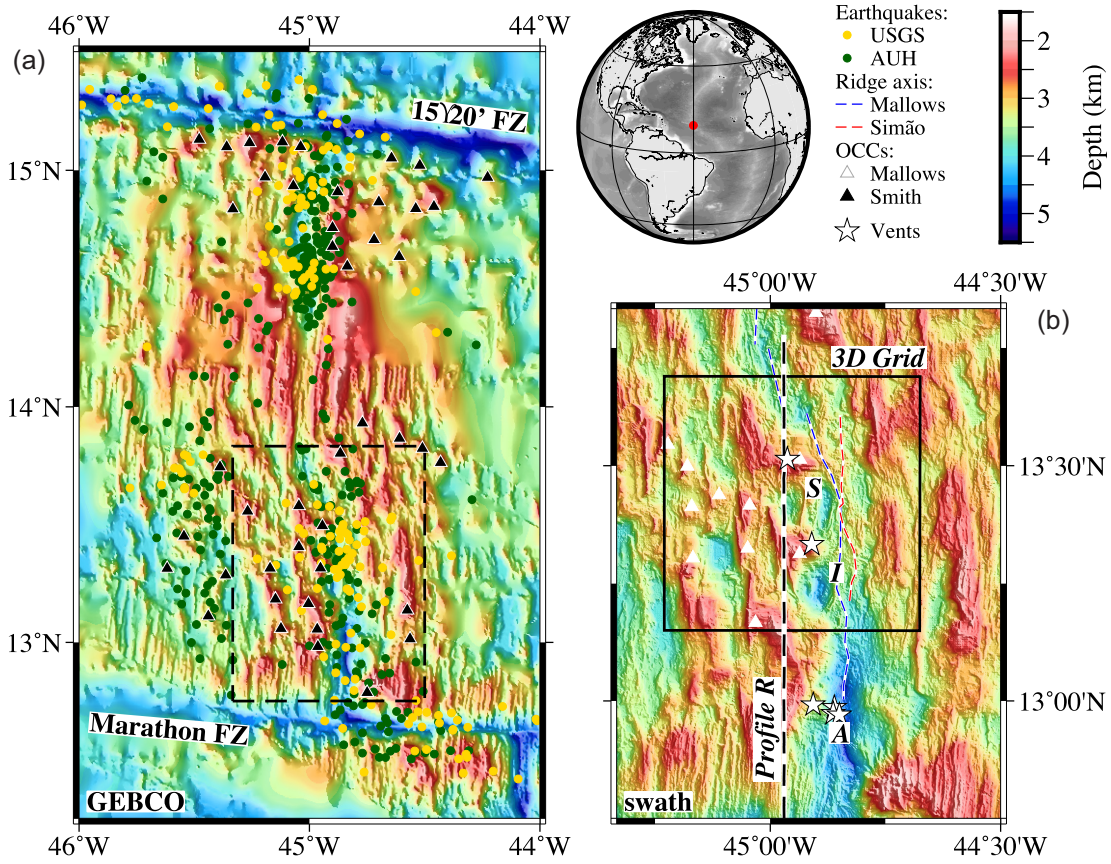

Figure 1. Bathymetry of the Fifteen-Twenty FZ-to-Marathon FZ segment of the Mid-Atlantic Ridge. (a) Regional bathymetry (GEBCO—https://www.gebco.net/) showing the tectonic and seismicity context of this study. Seismic events, recorded by the USGS (yellow circles—https://earthquake.usgs.gov/) and the Autonomous Underwater Hydrophone (AUH) array as presented in Escartín *et al.* (2003b—green circles), broadly define the location of the spreading centre and the bounding active transform faults. OCCs identified by Smith *et al.* (2006) are marked by solid black triangles. The footprint of the map shown in (b) is outlined by the dashed black line. (b) Swath bathymetry of the study area, showing the footprint of the 3-D grid model space (black line), as presented in Simão *et al.* (2020). The black dashed line represents the 2-D transect, Profile R, presented in Peirce *et al.* (2019a, 2020). The location of the spreading centre as determined by Mallows & Searle (2012) from backscatter analysis is marked by the blue dashed line, and by Simão *et al.* (2020) from a 3-D *P*-wave velocity–depth model by the red dashed line. Mallows & Searle's (2012) identified OCCs are marked by white triangles, while hydrothermal vent sites are marked by white stars with the Semyenov (S) at 1330, Irinovskoe (I) at 1320 and Ashadze Complex (A) fields labelled. Inset: Location of the study area in the North Atlantic.

(ii) High-resolution magnetic and swath bathymetry data acquisition by autonomous underwater vehicle (AUV) and shipboard equipment, to resolve 3-D structure and variation in spreading rate asymmetry along axis (Searle *et al.* 2019).

(iii) Seismic reflection and refraction data acquisition along a 2-D transect (Peirce *et al.* 2019a, 2020) and through a 3-D array of deployed OBSs (Simão *et al.* 2020) to determine *P*- and *S*-wave seismic velocity variations beneath, between and beyond adjacent OCCs and image the structural independence, or otherwise, of the detachment surfaces and reveal their broad-scale lithology and morphology from seabed to the uppermost mantle.

Here we describe the results of modelling the *S*-wave component of the 3-D active seismic experiment conducted during JC132 (Reston & Peirce 2016), over the same 60 × 60 km area (Fig. 1b) as the *P*-wave component reported by Simão *et al.* (2020). Within this footprint lies an active OCC located at 13°20′N, an OCC reaching the end of its life cycle at 13°30′N, an inactive but preserved OCC at 13°25′N, and the current spreading centre axis. Henceforth these OCCs will be referred to by their location—that is 1320, 1330 and 1325, respectively. Whilst Simão *et al.* (2020) used the *P*-wave arrivals within the 3-D data set to determine OCC structure, geometry and interconnectivity along axis, the co-incident *S*-wave data provides a unique opportunity to resolve outstanding questions of OCC lithology and degree of alteration (e.g. Mallows & Searle 2012; Peirce *et al.* 2020).

2 TECTONIC AND GEOLOGICAL CONTEXTS

The MAR (Fig. 1a) is broadly classified as a slow spreading ridge, although ultra-slow spreading segments are found in the North Atlantic (Dick *et al.* 2003; Muller *et al.* 2008). Such spreading rates are accommodated by widespread tectonic extension (e.g. Bergman & Solomon 1980, 1990; Escartín *et al.* 1999; Smith *et al.* 2003; Szitkar *et al.* 2019), with up to 35 per cent of present-day MAR accretion accounted for by detachment faulting alone (Smith *et al.* 2006). The MAR is divided into segments by transform faults (TFs) and fracture zones (FZs) that offset of the ridge axis (Hensen *et al.* 2019; Grevemeyer *et al.* 2021), by up to 900 km in the case of Romanche FZ. In the northern Atlantic the boundary between the

African and Eurasian plates occurs at the Gloria TF-FZ (Serpelloni *et al.* 2007; Batista *et al.* 2017), that is also observable in the seismological record (e.g. USGS catalogue—https://earthquake.usgs.gov). In contrast, the North and South American plates are not separated by a similar TF-FZ system running across the Atlantic, but instead by a band of ridge-parallel, sparse off-axis seismicity, suggesting that the plate boundary may be diffuse between the Fifteen-Twenty (15°20′N) and Marathon (12°45′N) fracture zones (Escartín *et al.* 2003b; Mallows & Searle 2012; Simão *et al.* 2020).

Within the Fifteen-Twenty-to-Marathon segment, the dominant mode of oceanic crustal formation varies. Hydrophone-recorded seismicity (Smith *et al.* 2002, 2003; Escartín *et al.* 2003b), and earthquakes from global catalogues (e.g. USGS catalogue), indicate that the northern portion of the segment is the most tectonically active section. Here the presence of typical abyssal hill structures is attributed to it being a faster, more symmetrically spreading, section of the segment (Fig. 1a). The northernmost portion, between 14°30′N and 15°20′N, has an intermediate depth (∼4.5 km) spreading centre and both abyssal hill and detachment structures are observed (Fig. 1a; Smith *et al.* 2008), although they are less well defined morphologically than along the other parts of the segment. This portion also hosts the Logatchev Massif and its accompanying hydrothermal vent field (Fujiwara *et al.* 2003; Grevemeyer *et al.* 2013). The northern section is offset from the classic abyssal hill fabric and shallower spreading centre (<3 km) observed between 13°45′N and 14°30′N, with the latter exhibiting little observed seismicity (e.g. Smith *et al.* 2002, 2003; Escartín *et al.* 2003b). This more magmatically-spreading section is bound to the south by a non-transform offset that accommodates an ∼15 km eastward shift in the spreading axis (Mallows & Searle 2012; Simão *et al.* 2020), which currently may be evolving into a small-offset transform fault (Simão *et al.* 2020). Between this incipient small-offset transform fault located at 13°45′N to Marathon TF-FZ, at 12°45′N, the active spreading centre displays a highly variable axial depth (3–5 km), with the seabed of the western flank dominated by OCCs (Mallows & Searle 2012; Fig. 1b). The spreading asymmetry along this section is estimated to be currently up to 40 per cent (MacLeod *et al.* 2009; Mallows & Searle 2012) but ∼30 per cent on average over the last ∼1.8 Myr (Searle *et al.* 2019).

South of 14°N along the MAR, Smith *et al.* (2008) identified 24 OCCs based on their characteristic outward-facing slopes, linear ridges and elevated corrugated surfaces (Fig. 1). Mallows & Searle (2012) document a further four inactive OCCs using side-scan sonar and high-resolution bathymetry data (Fig. 1). The axial detachments within the broader study area of this paper (Fig. 1b), comprise the Ashadze Complex at ∼13°00′N, and the 1320, 1330, and 13°48′N OCCs. All are well documented by MacLeod *et al.* (2009), with additional observations detailed by Mallows & Searle (2012). The 1320 and 1330 OCCs are the specific focus of this study, and their characteristics (MacLeod *et al.* 2009; Mallows & Searle 2012) are as follows:

1320 OCC—a detachment surface ∼11 km wide in the along spreading centre direction that accommodates ∼9 km of heave, significant spreading-parallel corrugations (strike 270°), and a thin veneer of sediment (Mallows & Searle 2012). This OCC is thought to have been active for ∼0.5 Myr (Simão *et al.* 2020), and accommodates the active Irinovskoe (Fig. 1b) black smoker vent system. Beneath the detachment surface lies a region of *P*-wave velocity (*Vp*) 1–2 km s^{-1} faster in the upper ∼2 km of crust than at equivalent depth beneath the spreading centre (Simão *et al.* 2020). Despite observations of extensive *in situ* peridotites across the domed surface (MacLeod *et al.* 2009), gravity modelling requires a relatively low density within the OCC itself of 2900 kg m^{-3} (typical unaltered peridotite density is 3300 kg m^{-3}) and, hence, was termed the Low-Density Zone (LDZ) by Mallows & Searle (2012). Similar, low density zones modelled at Atlantis Massif are proposed to be associated with either a serpentinization front (Nooner *et al.* 2003) or gabbroic intrusions (Ildefonse *et al.* 2007).

1330 OCC—a detachment surface ∼14 km wide displaying characteristic spreading-parallel corrugations that is thought to have been recently active (MacLeod *et al.* 2009; Mallows & Searle 2012). It hosts the Semyenov (Fig. 1b) white smoker vent system in the chaotic terrain to the west of the corrugated surface. Sediment cover is thicker than at 1320, as indicated by slightly lower and more consistent acoustic backscatter, and the detachment surface is cut by north–south trending faults that formed after the striations (Mallows & Searle 2012), and are associated with active seismicity (Parnell-Turner *et al.* 2021). These observations support the interpretation that this OCC is older than 1320 and is no longer actively forming (∼0.7 Myr–Simão *et al.* 2020). The *P*-wave velocity within the OCC is slower than within 1320, but remains >1 km s^{-1} faster than at an equivalent depth beneath the spreading centre (Simão *et al.* 2020). The LDZ is also thicker beneath 1330 than 1320, and may represent either a greater degree of serpentinization, more volumetric serpentinite (and/or other alteration lithologies), or more extensive intrusion of gabbro (Mallows & Searle 2012).

Located ∼25 km off-axis, the now inactive 1325 OCC lies in ∼2 Myr-old crust (Fig. 1b) in between the 1320 and 1330 OCCs. The detachment is extensively faulted and has a *P*-wave velocity, ∼1 km s^{-1} faster than beneath the spreading centre. Hummocky volcanic terrain, typical of a slow-spreading centre (e.g. Smith & Cann 1990), exists throughout the axial valley (Searle *et al.* 2019), and is cross-cut in places by approximately north-south trending faults. The spreading centre subseabed is associated with a lower *Vp* and greater crustal thickness (∼7 km) than beneath the 1320 and 1330 OCCs (∼5 km–Simão *et al.* 2020) and, from this characterization, the axial valley has been identified to be egg timer-shaped, that is wider where OCCs are absent and narrower in regions juxtaposing the toes of their detachment surfaces.

3 DATA ACQUISITION AND TRAVELTIME PICKING

Along the 13°N segment, a dense grid of 46 OBSs was deployed around the 1320 and 1330 OCCs (Fig. 2a), with wide-angle (WA) seismic data being acquired via the shooting of eight north–south and nine east-west transects across the deployed instrument array. OBSs and seismic profiles were spaced, on average, ∼5 km apart. Seismic data were recorded at a sampling rate of 250 Hz using a hydrophone and three orthogonal (x, y, z) geophone channels. Traces were recorded in 60 s windows to match the shot firing interval which, at a survey speed of ∼4.9 kn (∼2.5 m s^{-1}), resulted in an ∼150 m shot spacing. The seismic source was towed at ∼8 m depth and consisted of an array of 13 Bolt airguns of various chamber sizes, summing to give a total volume of 4800 in^3 (78.7 l). Shot and OBS deployment locations were determined using GPS. Further information on the active seismic acquisition is detailed in the cruise report (Reston & Peirce 2016) and by Simão *et al.* (2020).

This study focuses on the *S*-wave arrivals, with the *P*-wave arrivals having been tomographically modelled by Simão *et al.* (2020). OBS locations on the seabed were determined by Simão

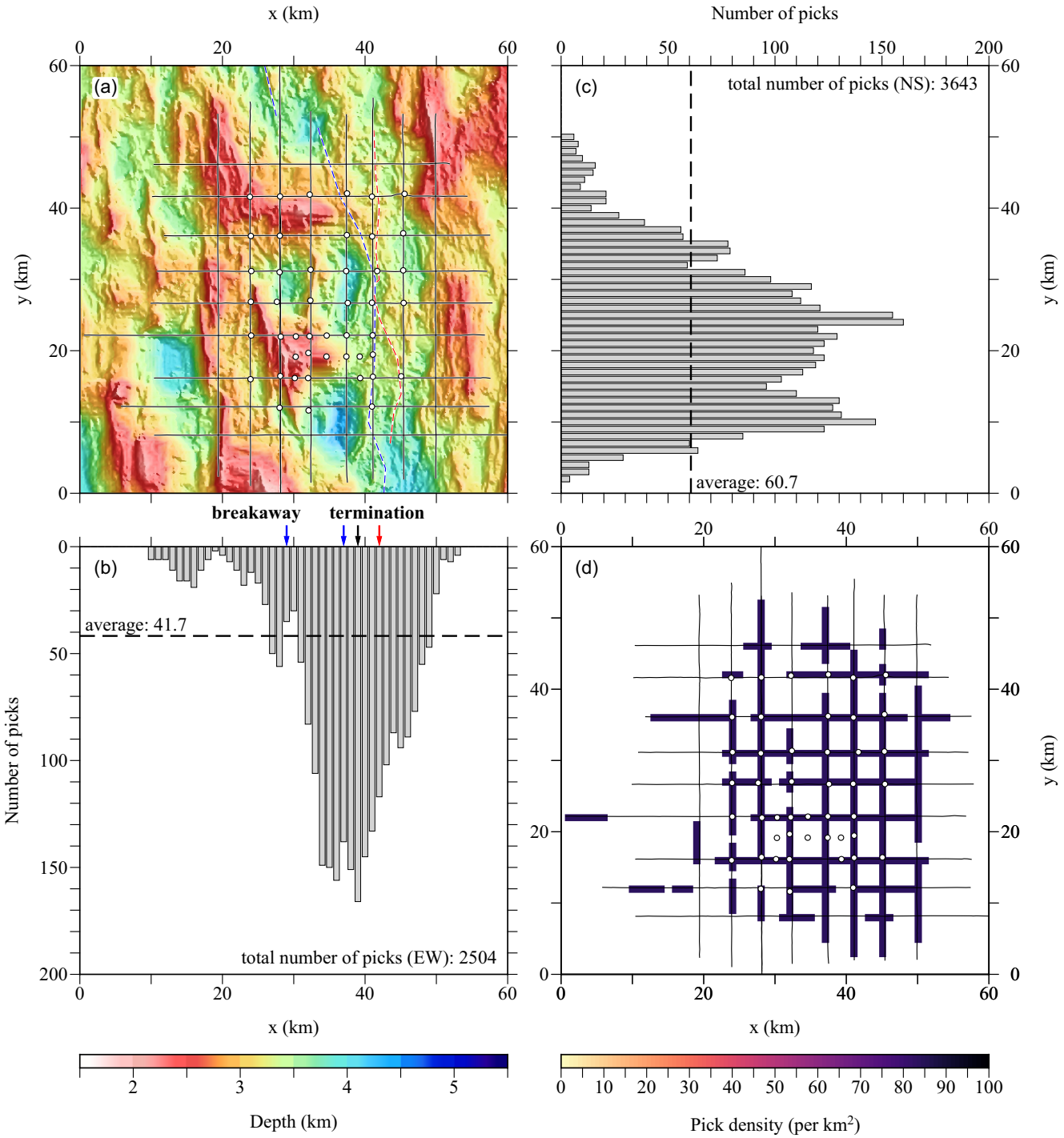

Figure 2. Acquisition geometry and traveltime pick statistics. (a) Bathymetric map of the 3-D grid footprint, showing shot profiles as solid black lines, OBS locations as white circles, and the location of the spreading centre proposed by Mallows & Searle (2012; blue dashed line) and Simão *et al.* (2020; red dashed line). (b) Histogram of *S*-wave traveltime picks within 1-km-wide bins, made from east–west (EW) orientated shot-receiver azimuths. The average location of the OCCs' breakaway and termination are indicated (blue arrows), and the average proposed spreading centre locations from Mallows & Searle (2012) and Simão *et al.* (2020) are shown by the black and red arrows respectively. (c) Histogram of picks within 1-km-wide bins, made from north–south (NS) orientated shot-receiver azimuths. (d) Pick density along each shot profile, showing that *S*-wave arrivals are more readily observed for shots fired to the east of the 1320 and 1330 OCCs and current spreading centre. Average pick density is shown in both histograms (b and c) as a black dashed line. There is a greater density of picks from NS than from EW orientated shot-receiver azimuths, and the EW orientated picks suffer a significant drop-off in density west of the average OCC termination.

et al. (2020), to better than 50 m, through ray-trace forward modelling, using *rayinvr* (Zelt & Ellis 1988; Zelt & Smith 1992), of water-waves propagating through a sound velocity profile-derived model of the water column. The low signal-to-noise ratio of the *S*-wave arrivals required pick times to be determined using a combination of geophone and hydrophone data record sections, and with a range of filters applied to best suit each instrument individually. No other data processing was applied. A total of 6147 *S*-wave arrivals were picked using all shots recorded by all OBSs, and are interpreted to have turned predominantly at upper-to-mid crustal depths. This represents approximately 1/20th of the ∼130 000 *P*-wave first arrivals picked by Simão *et al.* (2020) from the same acquisition geometry, and reflects the challenges of recording *S* waves at all in regions of unsedimented seabed. *S*-wave traveltime pick uncertainties were set at 100 ms, primarily to account for the significantly reduced signal-to-noise ratio compared to the *P*-wave arrivals. Representative example record sections for OBSs 23 and 39 (Figs 3 and 4) show the observed arrivals and the corresponding pick traveltimes and uncertainties, highlighting the difference between the *P*- and *S*-wave arrivals. Seabed topography is highly variable throughout the study area (Fig. 2a) and controls the trend of the arrival traveltimes as well as the significant drop-off in signal amplitude at increasing shot-receiver offsets.

There is a notable variation in the distribution of identified *S*-wave arrivals throughout the grid of profiles. Shot profiles with a north-south dominant shot-receiver geometry have an almost 1.5 times greater number of picks compared to those with an east-west dominant shot-receiver geometry (Fig. 2), as might be expected due to the seabed topography and signal scattering. The north-south pick histogram (Fig. 2c) displays a typical distribution, with pick density reducing towards the edges of the experimental footprint as would be expected, reflecting the greater shot-receiver coverage at the centre of the grid resulting from the larger number of instruments deployed around the 1320 OCC. Conversely, the east-west shot-receiver geometry histogram (Fig. 2b) deviates from the expected distribution, with a marked reduction in picks made to the west of the current spreading centre (Mallows & Searle 2012; Simão *et al.* 2020). The semblance of modelling of the coincident *P*-wave data set (Simão *et al.* 2020) demonstrates a similar geographical distribution, with improved anomaly recoverability to the east of 30 km (*x*-axis) in the model space (Fig. 2a). This correlation between *S*-wave data coverage and *P*-wave model recoverability, suggests that either the change in morphology or the underlying geological and lithological structure across the spreading centre has a significant control on the propagation of seismic energy through the subsurface (e.g. Sohn *et al.* 1997; Peirce & Day 2002).

4 TOMOGRAPHIC INVERSION

Tomographic modelling of the *S*-wave crustal structure was undertaken using *FAST* (First Arrival Seismic Tomography; Zelt & Barton 1998). *FAST* applies a regularized inversion, iteratively updating a smooth velocity grid, to minimize the residuals between observed and modelled traveltimes. This approach was used because it is widely applied to tomographic problems, generates a smooth velocity model independent of user bias, and provides a ready means to statistically test the goodness of fit to observed traveltimes and appraise anomaly recoverability. *FAST* was primarily chosen though, to be consistent with Simão *et al.* (2020), to make the models directly comparable and derived in the same manner and on the same basis.

The linearization assumption of *FAST* (Zelt & Barton 1998) requires that 'small perturbations to the starting model are determined'. While an initial velocity model can be designed to be a close approximation to typical oceanic crustal velocity–depth structure (e.g. Shaw 1994; Grevemeyer *et al.* 2018a), the inherent challenge of investigating an OCC-dominated region of oceanic crust is that it has significant lateral and vertical lithological variation, and thus also seismic velocity variation, over relatively small spatial areas. Despite this challenge of modelling abrupt lateral velocity gradients, apparently in conflict with a fundamental aspect of the inversion algorithm, Peirce *et al.* (2019a, 2020) demonstrated that *FAST* is capable of effectively recovering a smooth velocity model with strong lateral velocity variations that deviates significantly from the initial model.

4.1 Initial model construction

Simão *et al.* (2020) applied two modelling approaches to the *P*-wave inversion: one that maximized the model resolution in the upper-to-mid crust, where ray paths were at their greatest density (termed the *high resolution shallow model—HRSM*); and the other to sufficiently resolve velocity structure deeper in, and approaching the edges of, the model space where ray paths were more sparse (termed the *low resolution deep model—LRDM*). Our *S*-wave data set has a pick density that is significantly lower than that of the *P*-wave data set modelled by Simão *et al.* (2020) and, as such, we have followed the initial model setup used for the *LRDM* and adopted a forward node spacing of 0.5 km both laterally and vertically. The seabed within all models was constructed by sampling the swath bathymetry data grid.

Two types of initial model were tested. The first was based on Simão *et al.*'s (2020) *LRDM* initial model (Fig. 5a), which was converted from *P*- to *S*-wave velocity equivalent using a *Vp*/*Vs* ratio of 1.7. This conversion ratio is relatively low, and more typical of magmatically accreted oceanic crust. However, this approach was chosen so that, to achieve higher *Vp*/*Vs* ratios representative of serpentinization or faulting that might be expected associated with OCCs, it would force the inversion to iterate away from its initial state based on the observed traveltime picks. This *sea surface parallel initial model* (Fig. 5c) was defined by a 1-D velocity–depth profile starting at the sea surface, with *S*-wave velocity increasing from 1.5 to 4.5 km s^{-1} at ∼8-km-depth below sea surface (bss), thus effectively representing a constant-depth Moho starting point. The second type of initial model tested was based on a sample through Simão *et al.*'s (2020) *LRDM* inversion model (Fig. 5b) at grid position $x = 42$ km, $y = 30$ km (the 'difference' point of Simão *et al.* 2020—see their fig. 7), again converted to *S*-wave velocity using a *Vp*/*Vs* ratio of 1.7. This *seabed following initial model* (Fig. 5d) has velocity contours that mirror the bathymetry, thus effectively representing a fixed crustal thickness starting point. With modelling parameters remaining fixed between runs, statistically similar final models with comparable fits were achieved for each of these initial model types, suggesting that the choice of starting model structure does not significantly affect, or control, the outcome of the modelling process overall.

Here, we present the results of modelling using the *sea surface parallel initial model* (Fig. 5c), as this ultimately resulted in the lowest model misfit and is directly comparable to the modelling

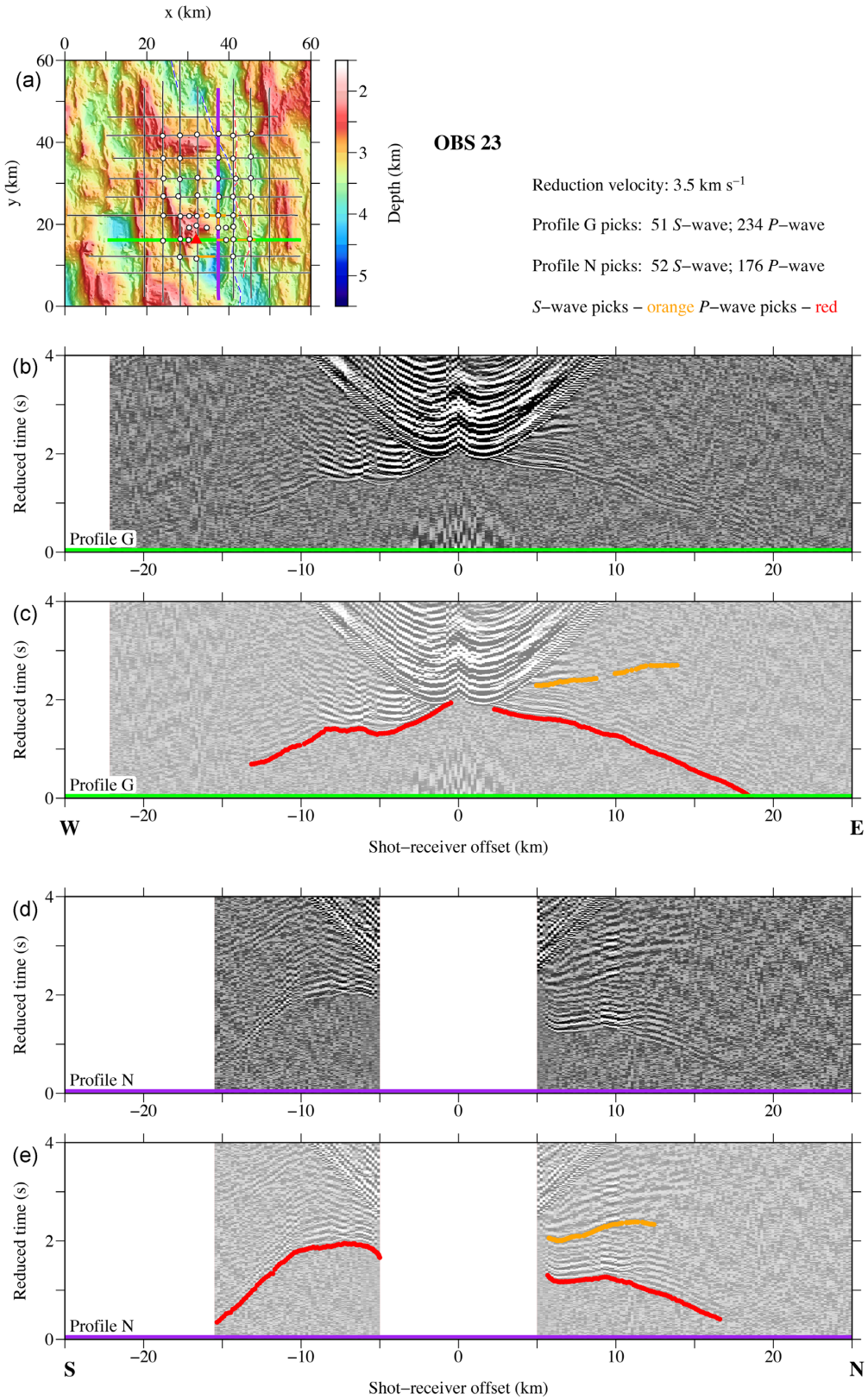

Figure 3. Example hydrophone record sections for OBS 23, bandpass filtered at 1-2–24-36 Hz. (a) Bathymetric map of the 3-D grid footprint, showing the experimental setup, with the OBS and shot lines indicated by a red inverted triangle and green (b and c) and blue (d and e) lines, respectively. Locations of *S*-wave traveltime picks made for this OBS are shown in orange. (b) Hydrophone record section along an east-west profile (Profile G) with *S*-wave traveltime picks shown in (c) as vertical orange bars whose height corresponds to the 100 ms pick uncertainty. Red vertical bars are the same as in Simão *et al.* (2020), representing *P*-wave traveltime picks with uncertainties of 50–75 ms. (d) and (e) are as in (b) and (c) but for a north–south profile (Profile N). All record sections are reduced at 3.5 km s^{-1} to show both *P*- and *S*-wave traveltime picks.

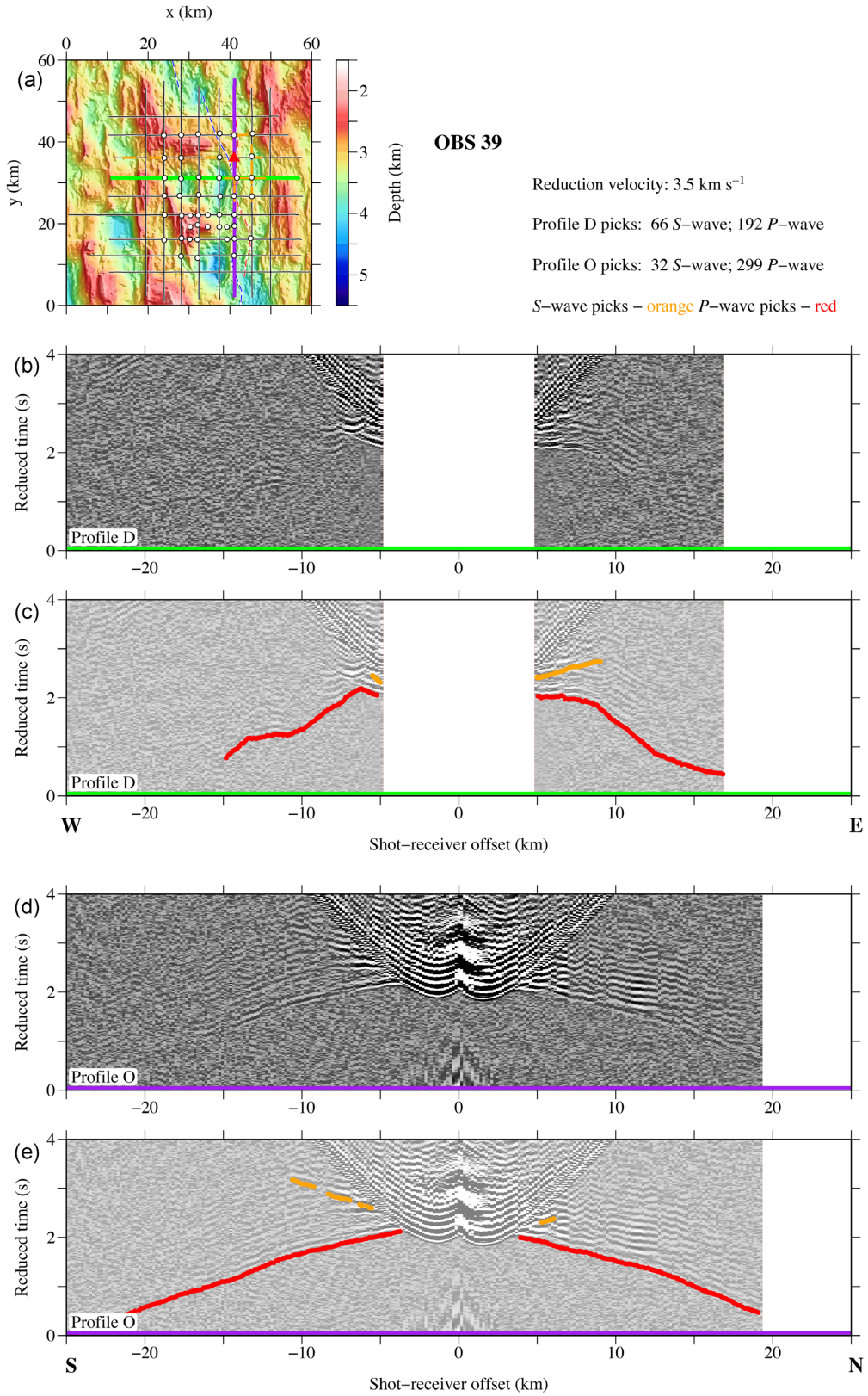

Figure 4. Example hydrophone record sections for OBS 39, bandpass filtered at 1–2-24–36 Hz. (a) Bathymetric map of the 3-D grid footprint, showing the experimental setup, with the OBS and shot lines indicated by a red inverted triangle and green (b and c) and blue (d a e) lines, respectively. Locations of *S*-wave traveltime picks made for this OBS are shown in orange. (b) Hydrophone record section along an east–west profile (Profile D) with *S*-wave traveltime picks shown in (c) as vertical orange bars whose height corresponds to the 100 ms pick uncertainty. Red vertical bars are the same as in Simão *et al.* (2020), representing *P*-wave traveltime picks with uncertainties of 50–75 ms. (d) and (e) are as in (b) and (c) but for a north–south profile (Profile O). All record sections are reduced at 3.5 km s^{-1} to show both *P*- and *S*-wave traveltime picks.

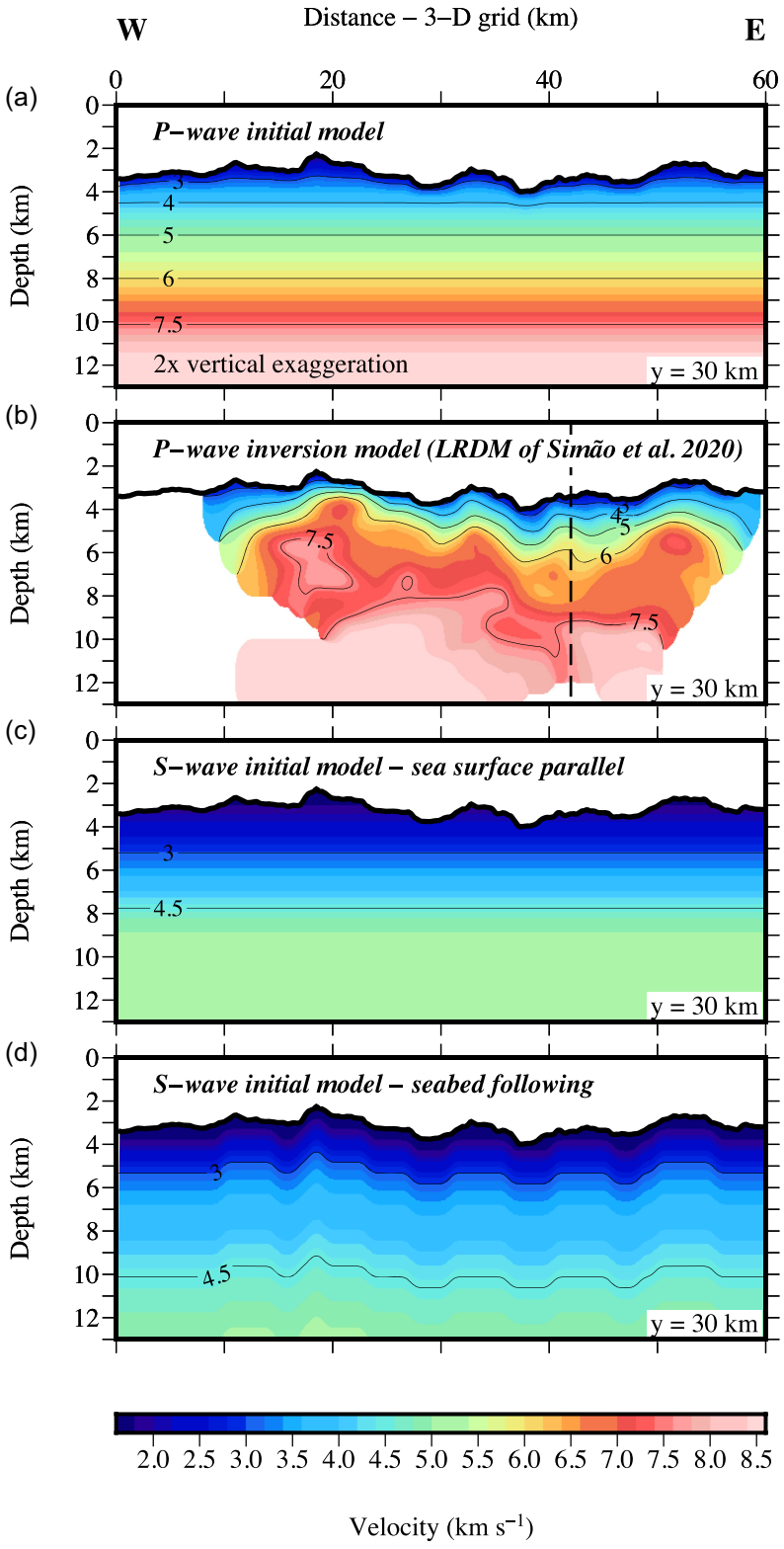

Figure 5. Vertical slices through the initial models of the *P*-wave (Simão *et al.* 2020) and *S*-wave 3-D inversions. (a) Vertical slice through the *P*-wave initial model, running through the inter-OCC basin and across the spreading centre (at model $y = 30$ km), showing the 1-D velocity–depth structure starting point of the *LRDM inversion model*. (b) Corresponding slice through the *LRDM inversion model*. The vertical dashed line marks the location of the sample used to create the *S*-wave *seabed following initial model*. (c) Corresponding slice through the *S*-wave *sea surface parallel initial model*. (d) Corresponding slice through the *S*-wave *seabed following initial model*. See text for details of initial model construction. The 4.5 km s^{-1} *S*-wave velocity contour is used as the proxy for the crust-to-mantle transition, based on Simão *et al.* (2020).

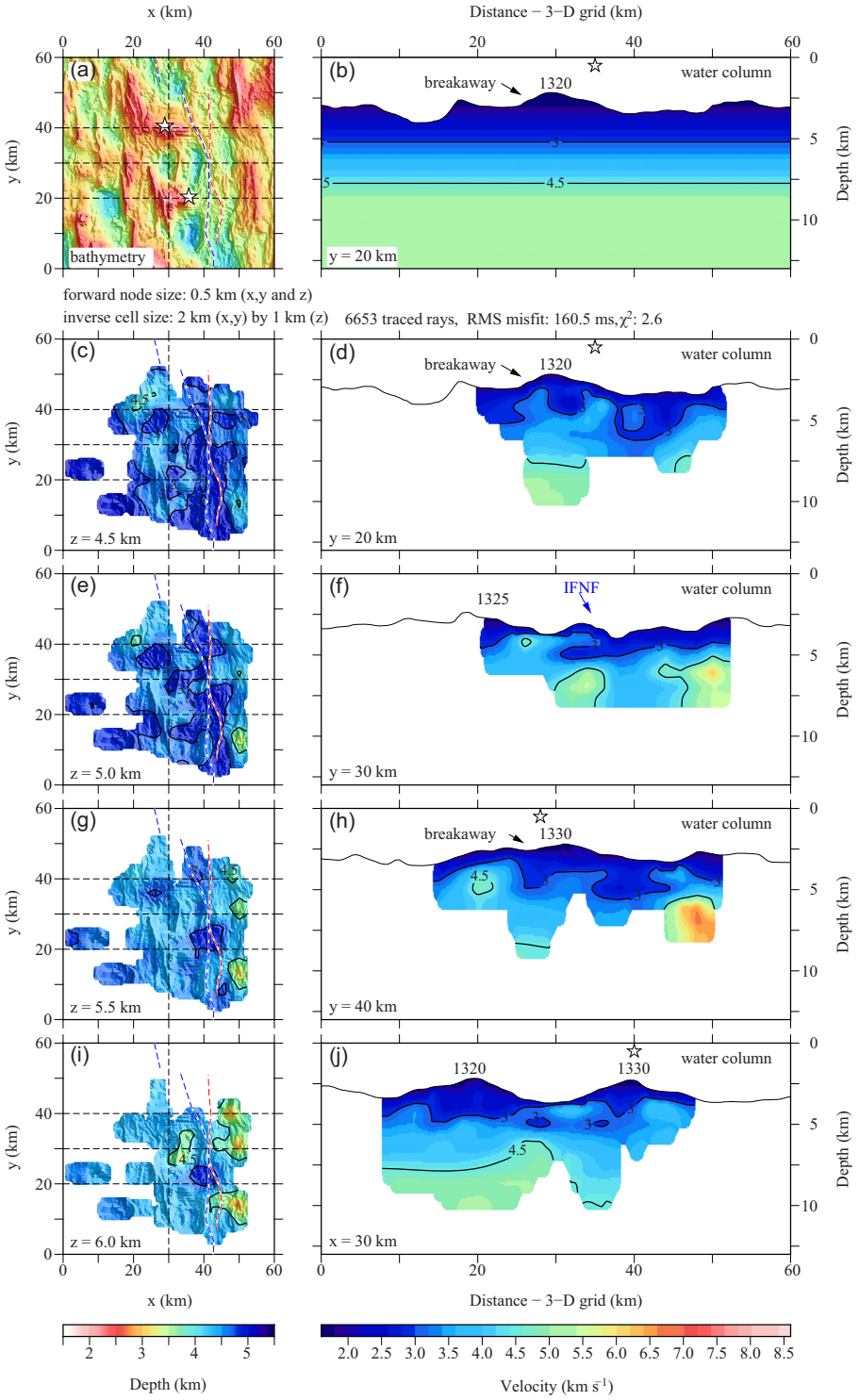

Figure 6. Slices through the 3-D *S*-wave *inversion model* derived using the *sea surface parallel initial model* (Fig. 5). (a) Bathymetry map showing the proposed spreading centre from Mallows & Searle (2012—blue dashed line), and Simão *et al.* (2020—red dashed line), together with the location of active vent sites (white stars). Black dashed lines in (a) and in all horizontal (depth) slices indicate the locations of the vertical slices through the velocity model. (b) Vertical slice through the *sea surface parallel initial model* (Fig. 5) at $y = 20$ km with the location of the 1320 OCC and its breakaway annotated. (c) Depth slice through the *inversion model* at z = 4.5 km bss. (d, f, h and j) Vertical slices through the *S*-wave *inversion model* at the annotated model distances and with relevant features annotated. IFNF—inward-facing normal fault of Simão *et al.* (2020). (e, g and i) Depth slices through the *inversion model* at the annotated model depths bss. In all *inversion model* parts, the 3.0 and 4.5 km s^{-1} *S*-wave velocity contours are annotated, and the slices are masked using the *inversion model* ray coverage. The corresponding hit count, used to demonstrate the ray coverage and define the mask, is provided as Fig. S1. The 4.5 km s^{-1} *S*-wave velocity contour is used as the proxy for the crust-to-mantle transition, based on Simão *et al.* (2020). Depth slices are illuminated by the seabed topography. Model parameters, the number of traveltime picks included in the ray tracing, and the resulting χ^2 and RMS misfit are indicated. An alternative version of this figure based on the 3-D *S*-wave *inversion model* derived using the *seabed following initial model* is provided as Fig. S2.

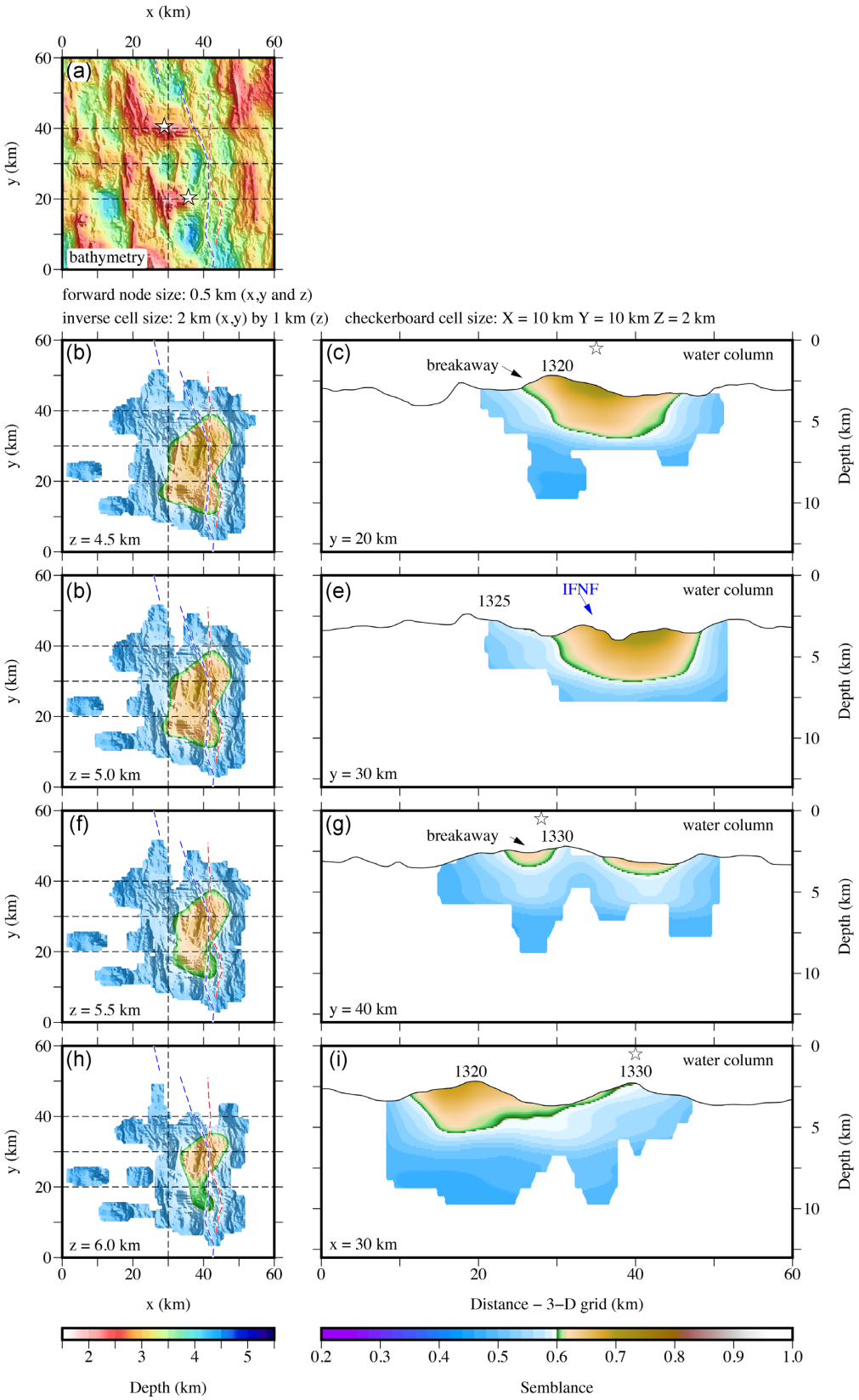

Figure 7. Slices through the *semblance model* derived from checkerboard testing of the 3-D *S*-wave *inversion model* (Fig. 6) resulting from the *sea surface parallel initial model* (Fig. 5). Each of the slices represents the semblance based on averaging the result of the 32 possible permutations of a 10 × 10 × 2 km checkerboard. The 0.7 semblance contour is used to indicate where model recoverability (resolution) is considered good (Zelt 1998). See Fig. 6 for details of each slice. An alternative version of this figure based on the 3-D *S*-wave *inversion model* derived using the *seabed following initial model* is provided as Fig. S3.

process adopted by Simão *et al.* (2020). The results of modelling using the *seabed following initial model* (Fig. 5d) are included in the Supporting Information for comparison. In all models, seismic waves were assumed to convert between compressional and shear waves at the seabed. Whilst this might be simplistic, as *P*-to-*S*-wave mode conversion could occur at any interface, and conversion is less efficient at rough surfaces with a high Poisson's ratio in the underlying layer (Spudich & Orcutt 1980; Collier & Singh 1998), it is the only scenario that can be modelled considering all of the modelling constraints. The very thin, <10 m thick, sediment cover (Mallows & Searle 2012) is insufficiently thick to be modelled by *FAST* when the model forward node spacing is set to 0.5 km both laterally and vertically, and so is excluded with negligible effect on the modelling errors and assumptions.

4.2 Modelling procedure and parametrization

All modelling parameters were systematically tested to ensure that the final model (henceforth *inversion model*) had minimal artefacts and the lowest misfit within the limitations of the data and modelling approach adopted. The initial model was inverted over six iterations, with six values of the trade-off parameter (λ), which controls the minimization of data misfit compared to the minimum required structure, following the process of Simão *et al.* (2020). Starting trade-off parameter ($\lambda 0$) values of between 20 and 100 resulted in comparable final models. The model smoothness factor (Sz), which controls the ratio of vertical to horizontal smoothing, when set to 0.3, resulted in few modelling artefacts and the lowest residuals. Model edge constraints were removed (sedge = 0) to allow the inversion the freedom to update the edges away from the initial velocity structure, as the model was not based on a known velocity structure, and because the model edges have minimal or no constraint from traveltime picks (Fig. 2). The only significant change in modelling parametrization from that adopted by Simão *et al.* (2020) was to increase the inverse grid size, from 1.5 × 0.5 km to 2.0 × 1.0 km (lateral size × vertical size), to accommodate the lower pick density in the *S*-wave data set. The final parameters chosen, which result in a velocity model absent of significant velocity artefacts and with the lowest misfit to the data, are presented in Table 1 alongside those from Simão *et al.* (2020).

When compared to both Simão *et al.*'s (2020) *HRSM* and *LRDM* ($\chi^2 = 1.0$ and 1.3, respectively), the statistical fit achieved by our *S*-wave inversion (Fig. 6) is not as good ($\chi^2 = 2.6$), even accounting for the increased pick uncertainty. This unsurprising outcome results from there being a low pick density and an uneven spread of picks, which produces both a large model 'edge' relative to the total model volume and, in some model regions, laterally isolated banding (e.g. between $0 < x < 25$ km and $0 < y < 30$ km—e.g. Fig. 6i). Where isolated regions of the model are recovered, the inversion algorithm is less able to optimize the fit to the observed traveltimes as smoothing of the surrounding background velocity limits the magnitude of change between iterations. Given this, we consider that the model misfit ($T_{RMS} = 160.5$ ms; $\chi^2 = 2.6$) is appropriate for the *S*-wave pick data set, which is characterized by lower signal-to-noise ratio and greater pick ambiguity, with picks more geographically restricted in distribution than is the case for the coincident *P*-wave pick data set (Simão *et al.* 2020). The results of modelling will be discussed in Section 5.

4.3 Resolution testing

Testing of the *inversion model*'s velocity–depth structure anomaly resolution was undertaken using the checkerboard method of Zelt & Barton (1998) and Zelt (1998), again to be consistent with and results directly comparable to that of Simão *et al.* (2020). This approach determines the degree to which a known velocity anomaly is recovered from the same inversion parameters and acquisition geometry used to develop the *inversion model*. Test checkerboard anomaly patterns were generated by applying a ±5 per cent maximum velocity perturbation to the *inversion model*. Synthetic traveltimes were calculated through this checkerboard model for the location of each observed traveltime pick (Fig. 2), with random Gaussian noise added based on the user-defined pick uncertainty (100 ms). The *inversion model* (Fig. 6) was then inverted using these calculated traveltimes and identical parameters to those in the inversion itself (Table 1). The degree to which the input checkerboard anomaly was recovered was appraised using the Zelt (1998) semblance parameter, with model regions with values ≥0.7 considered well recovered (Fig. 7). Checkerboard sizes were varied over a range of horizontal and vertical scales, assuming equal length in both horizontal (*x* and *y*) directions, to conduct a range of tests to determine the smallest possible resolvable velocity anomaly within the model space. These tests included lateral pattern sizes of 5–20 km and vertical sizes of 1–5 km and, for each pair within these ranges, checkerboard shifts of half-cell sizes were also tested to mitigate against testing biases of anomaly location and polarity (Zelt 1998; Zelt & Barton 1998). The semblance volumes from each of these tests, 32 in total, were averaged to produce a smoothed and objective quantification of model recoverability—henceforth the *semblance model* (Fig. 7).

Checkerboard testing suggests that the *inversion model* is capable of resolving 10 × 2 km (lateral × vertical), ±5 per cent velocity anomalies within a footprint spanning 30–50 km along the 3-D grid *x*-axis and 10–40 km along the *y*-axis (Fig. 7), covering both the 1320 OCC and inter-OCC region to at least 6-km-depth bss. However, this lateral resolution is equivalent to the footprint of an individual OCC, and so the *inversion model* can only be interpreted in terms of understanding their bulk morphology and lithology. Smaller checkerboard tests, such as 5 × 5 × 1 km and 5 × 5 × 2 km, indicate that less extensive velocity anomalies may be recoverable within the model space, but that these are laterally limited, shallow and typically focussed beneath or around the 1320 OCC, corresponding to the densest ray coverage of anywhere in the model space. In all checkerboard tests, model resolvability is limited to depths shallower than ∼7 km bss, ∼4 km below seabed (bsb), which suggests that, for typical magmatic crust (White *et al.* 1992; Dick *et al.* 2003; Grevemeyer *et al.* 2018a) or crustal thicknesses at slow-spreading centres (>5 km—Dick *et al.* 2003), the base of crust (Moho) or uppermost mantle is not constrained by our *inversion model*. Checkerboard testing also shows, as might be expected, that the resolution is significantly lower than that of the *HRSM P*-wave model (Simão *et al.* 2020), in which velocity anomalies 3 × 2 km (lateral × vertical) in size are recoverable to ∼6-km-depth bss. However, the *LRDM* recovers features 10 × 2 km in size to depths >7 km bss, equivalent to the *Vs inversion model* but laterally more extensively, which is an expected outcome given the ∼20 times higher number of *P*-wave traveltime picks. In summary, the *Vs inversion model* resolvability enables determination of the bulk composition and structure of whole OCCs, as well as those features that either join or separate them (Smith *et al.* 2006,

Table 1. Modelling parameters, and comparison with Simão *et al.* (2020). Forward model nodes are equally spaced in all model dimensions, whilst inversion grid cells are spaced equally in lateral dimensions, but can have a varying vertical dimension (listed as horizontal × vertical). Other parameters are as described in text.

Model	Forward model node spacing (km)	Inversion grid spacing (km)	Perturbation weighting factor, α	Trade-off parameter, λ	Smoothness factor, Sz	Edge constraint, Sedge	T_{RMS} (ms)	χ^2
This study	0.50^{lv}	$2.0^{l} \times 1.0^{v}$	0.9	0.31	0.300	0.000	160.5	2.6
HRSM[#]	0.25^{lv}	$0.75^{l} \times 0.25^{v}$	0.9	1.24	0.125	0.125	74.5	1.0
LRDM[#]	0.50^{lv}	$1.5^{l} \times 0.5^{v}$	0.9	0.44	0.125	0.125	84.7	1.3

l—lateral spacing; v—vertical spacing.
[#]Simão *et al.* (2020)

2008; MacLeod *et al.* 2009; Reston 2018), which is the aim of this study.

5 MODELLING RESULTS

Inversion modelling of the *S*-wave data set resulted in a velocity model that resolves large-scale structure within the upper-to-mid crust beneath the 1320 OCC, between that and the 1330 OCC, and beneath most of the current spreading centre only (Fig. 6). It is also directly comparable to the *S*-wave model of Peirce *et al.* (2020) along the 2-D transect (Profile R) which traverses, north–south, the 1320 and 1330 OCCs (Fig. 8). However, despite this lateral limitation, the *inversion model* can still be combined directly with the *LRDM* of Simão *et al.* (2020) to create a *Vp*/*Vs model* (Fig. 9), that should provide insight into bulk variation in lithological characteristics such as composition, porosity and crack aspect ratio (e.g. Shearer 1988; Wilkens *et al.* 1991; Grevemeyer *et al.* 2018a, b; Peirce *et al.* 2020).

To better highlight the lateral *S*-wave velocity variation, the difference (henceforth the *difference model*) between the *inversion model* and a reference crustal structure was also constructed (Fig. 10) by sampling the former at $x = 42$ km, $y = 30$ km, which lies at the spreading centre between 1320 and 1330 in a region where the seabed is covered by lava flows and volcanics and, thus, is interpreted to be currently magmatically active. The 1-D spreading centre sample was draped beneath the seabed to create the *reference model* for the entire 3-D grid, and this model was subtracted from the *inversion model* to show where the crustal structure differs from that resulting from magma-dominated accretion. This point was also chosen to be consistent with Simão *et al.* (2020) who used it as the reference point for their *P*-wave difference model, making features of that directly comparable with those of the *S*-wave *difference model* presented here.

5.1 *Vs* model structure

Across the model space the inversion iterated to increase the velocity from that of the initial model (Fig. 5) as anticipated. In general terms, vertical slices through the *inversion model* (Figs 6d, f, h and j) and *difference model* (Figs 10d, f, h and j) indicate quite laterally variable velocity in the subsurface, with distinct and separate regions of low *Vs* (2–3 km s^{-1}—*cf.* White *et al.* 1992) beneath 1320 and 1330 (Fig. 6j). Beneath the inter-OCC basin, the *S*-wave velocity is higher than the surrounds while, beneath the spreading centre, it is lower than at equivalent depth adjacent to the toe of either OCC. Only the ridgeward side of 1325 is imaged, but between that and the inward-facing normal fault that links the two OCCs (IFNF in Figs 6f and 10f), the upper crust has a higher *S*-wave velocity than elsewhere within the better resolved areas of the *inversion model*.

5.1.1 1320 and 1330 OCCs

The low *Vs* regions beneath the OCCs span >10 km laterally and remain below 3 km s^{-1} to ∼4 km bsb beneath 1320 and ∼3 km bsb beneath 1330. Caution needs to be taken when considering 1330, as the features modelled here are at the limits of model resolvability (Fig. 7). However, Peirce *et al.* (2020—their fig. 7) also resolve regions of comparably low *Vs* (<3 km s^{-1}) in the ∼2 km bsb along the 2-D Profile R ($x = 28$ km; Fig. 8). However, these are located beneath the breakaways of 1320 and 1330, which lie ∼2 km west of the low *Vs* structures recovered by the 3-D grid, but within the latter's lateral resolution. The *inversion model* is based on in- and out-of-the-plane crossing ray paths, and is not the assumption that all recorded arrivals come from within the plane as is the case with 2-D, which could explain this offset. However, the offset could equally result from anisotropy within the crust and, whilst this may be expected for an area of such geological complexity, the *S*-wave data set is insufficiently dense and the model too poorly resolved to investigate this further. Higher relative *Vs* (>3 km s^{-1}) is modelled to within 1 km of the seabed in the areas surrounding the OCCs, notably beyond the OCC breakaways to the west, the active spreading centre to the east, and the inter-OCC basin. The regions of higher *Vs* extend from the seabed to the maximum depth subseabed resolved by modelling. Given that the OCCs themselves, by definition, exhume gabbros and peridotites of the lower crust and upper mantle, this contrasting *Vs* pattern suggests that either these exhumed rocks are highly altered, are extensively faulted and fractured, have a high degree of permeability and/or porosity, have pervasive hydrothermal circulation, or a combination of these.

5.1.2 Inter-OCC region

Throughout the thickness of crust constrained by the modelling, the *S*-wave velocity is higher beneath the inter-OCC basin than elsewhere to the west of the spreading centre, particularly so between 1325 and the inward-facing normal fault that has a significant elevation at the seabed (located at $x = 34$ km, e.g. in Fig. 8a). Simão *et al.*'s (2020) interpretation of the *P*-wave inversion model suggests that the crust here formed as a result of magma rich accretion subsequent to the active life cycle of 1325 being concluded by an injection of magma at or in the vicinity of the (then) spreading centre. The *difference model* in this region (Fig. 10f) also suggests that the spreading ridge may have been more magmatically active until the inward-facing normal fault formed, than subsequently since it started migrating away from the ridge axis.

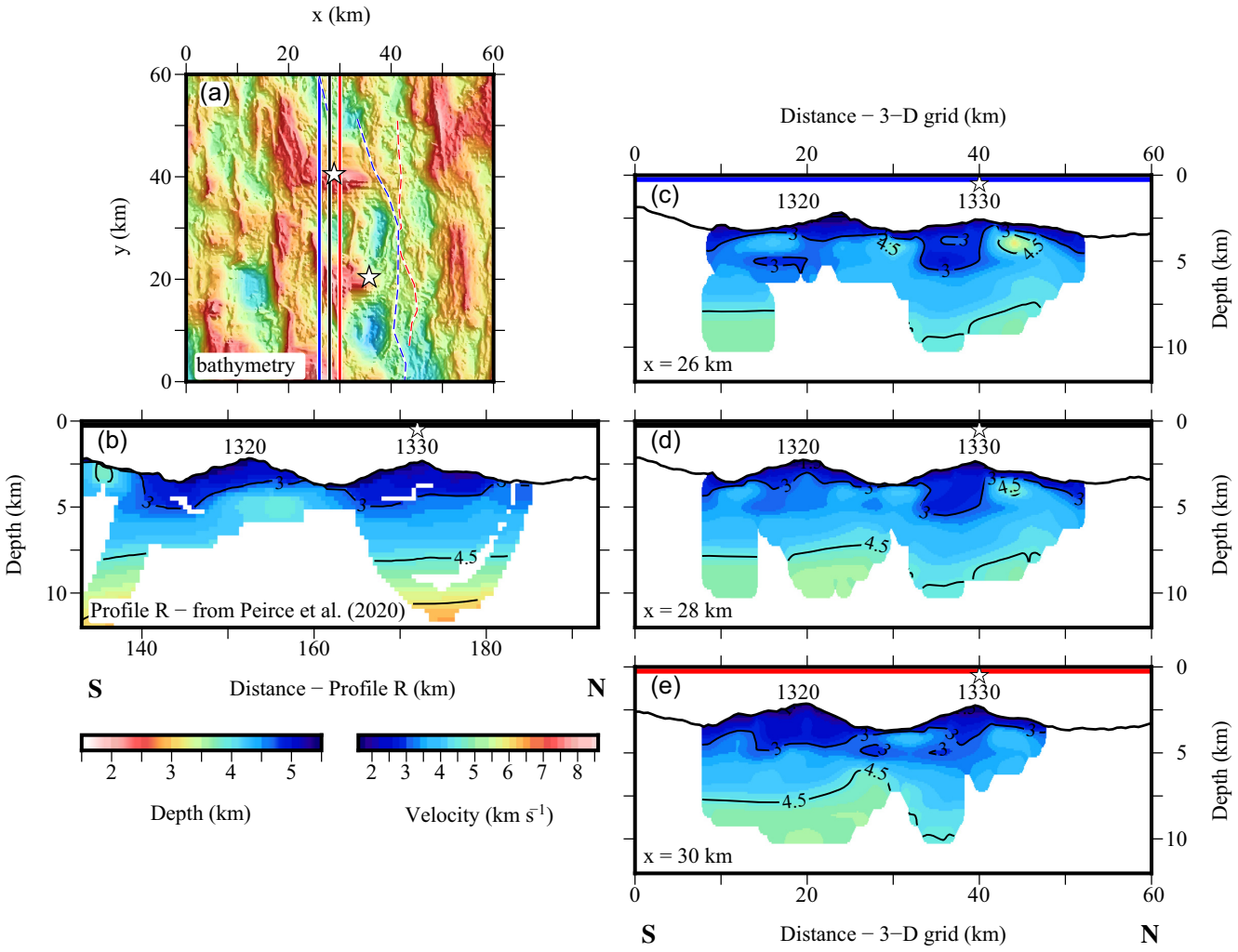

Figure 8. Comparison of the 3-D *S*-wave *inversion model* (Fig. 6), derived using the *sea surface parallel initial model* (Fig. 5), with that of the 2-D transect Profile R (Peirce *et al.* 2020). (a) Bathymetry map showing the proposed spreading centre from Mallows & Searle (2012—blue dashed line), and Simão *et al.* (2020—red dashed line), together with the location of active vent sites (white stars). The location of the profiles shown in (b-e) are indicated by their respective colours. (b) Profile R *S*-wave *inversion model* (Peirce *et al.* 2020), which crosses the southern edge of 3-D grid (*y*-axis = 0 km) at ∼133 km along profile. (c–e) NS trending profiles through the 3-D *S*-wave *inversion model* (Fig. 6), spaced at 2 km intervals ($x = 26$, 28 and 30 km). The model slice at $x = 28$ km (d) is coincident with Profile R (b), although the two show moderately different velocity structures beneath the OCCs. However, the model slice at $x = 30$ km (e) has a closer visual fit, with low *Vs* in the upper crust beneath the OCCs and higher *Vs* in the inter-OCC basin and surrounding area. Vertical slices (b–e) are masked using the ray coverage. See Fig. 6 for details. An alternative version of this figure based on the 3-D *S*-wave *inversion model* derived using the *seabed following initial model* is provided as Fig. S4.

5.1.3 Spreading centre

The *S*-wave velocity variation along the spreading centre is best interpreted by considering depth slices taken through both the *inversion* (Figs 6c, d, g and i) and *difference* (Figs 10c, d, g and i) *models*. Both Mallows & Searle (2012) and Simão *et al.* (2020) locate the axis of spreading; the former, based on seabed morphology, lies further east than the latter, based on *P*-wave velocity. Compared to the reference point, the velocity is consistent along axis in the very near surface (Fig. 10c). However, with increasing depth, and increasing distance away from the reference point both north and south, the *S*-wave velocity reduces and this lower velocity region widens, becoming egg timer-shaped in footprint. The Simão *et al.* (2020) *P*-wave-derived spreading centre generally demarks the western edge of this zone, while the Mallows & Searle (2012) seabed morphology-derived spreading centre delineates its centre. If the reference point lies in a region of active magmatic accretion as the *P*-wave model suggests, then this pattern of *S*-wave velocity variation may indicate that tectonism, and the permeability that it generates, is the predominant controlling factor in determining the *S*-wave crustal velocity. In turn, Simão *et al.*'s (2020) *P*-wave velocity variation may then, instead, reflect where that permeability becomes effectively closed.

5.2 *Vp*/*Vs* ratio

While measurements of *Vp* are often used exclusively to infer changes in lithology, when combined with coincident measurements of *Vs*, the resulting *Vp*/*Vs* or Poisson's ratio (σ) can be used as a seismic proxy for lithology, porosity and degree of alteration (e.g. Christensen 1996). In the oceanic crustal setting, Grevemeyer *et al.* (2018a) proposed using a *Vp*/*Vs* ratio of 1.9 to distinguish, at ultra-slow spreading centres, between magma poor crustal formation

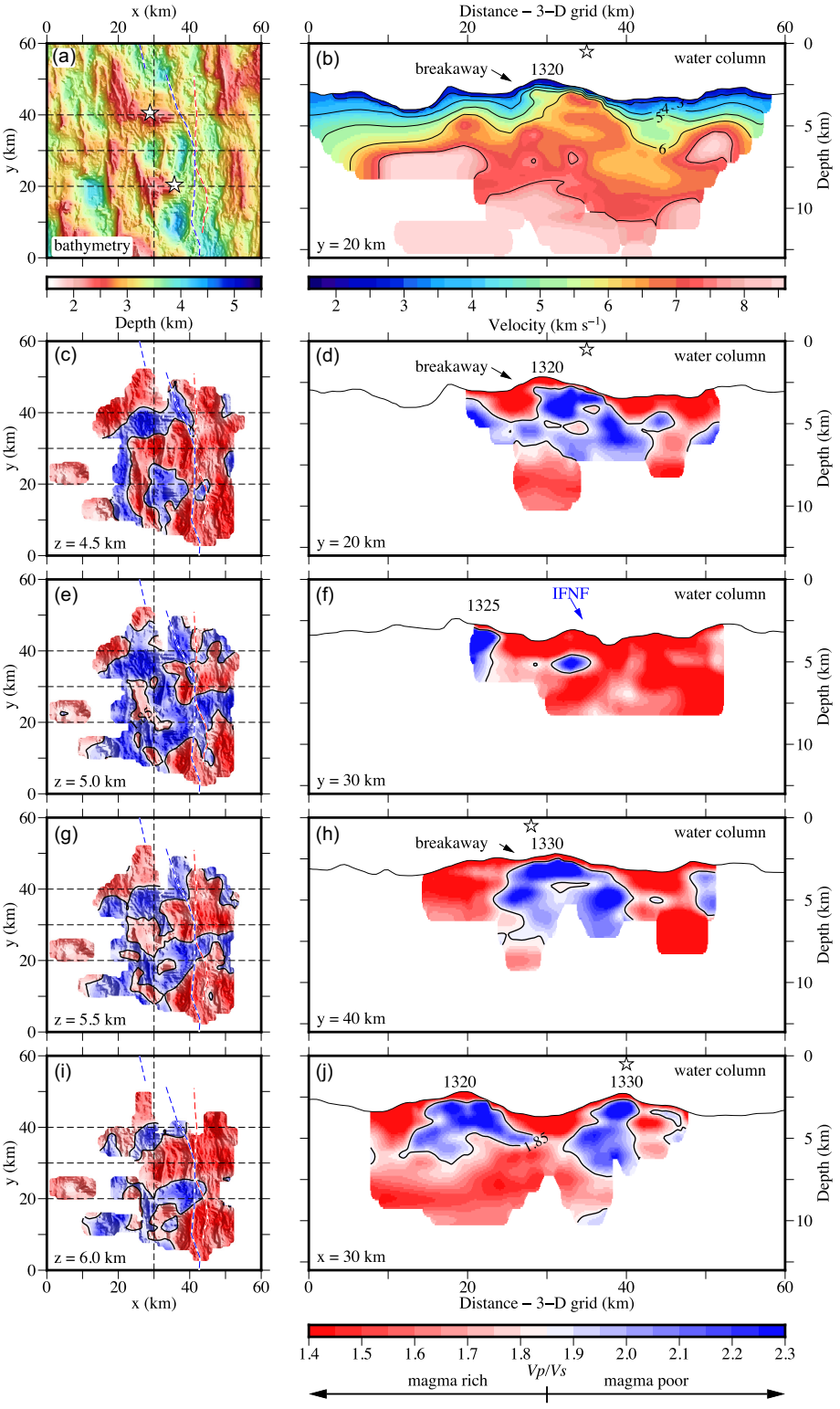

Figure 9. Slices through the *Vp*/*Vs model* calculated using the *P*-wave *inversion model* (*LRDM*–Simão *et al.* 2020) and the *S*-wave *inversion model* (Fig. 6) derived from the *sea surface parallel initial model* (Fig. 5). (a) Bathymetry map showing the proposed spreading centre from Mallows & Searle (2012—blue dashed line), and Simão *et al.* (2020—red dashed line), together with the location of active vent sites (white stars). Black dashed lines in (a) and in all horizontal (depth) slices indicate the locations of the vertical slices through the velocity model. (b) Vertical slice through the *P*-wave *inversion model* (Simão *et al.* 2020) at $y = 20$ km with the location of the 1320 OCC and its breakaway annotated. The equivalent for the *S*-wave *inversion model* is shown in Fig. 6d. (c) Depth slice through the *Vp*/*Vs model* at $z = 4.5$ km bss. (d, f, h and j) Vertical slices through the *Vp*/*Vs model* at the annotated model distances and with relevant features annotated. (e, g and i) Depth slices through the *Vp*/*Vs model* at the annotated model depths bss. In all *Vp*/*Vs model* parts, the 1.85 *Vp*/*Vs* contour is annotated (Peirce *et al.* 2019b, 2020), and the slices are masked using the *inversion model* ray coverage. See Fig. 6 for details of each slice. An alternative version of this figure based on the 3-D *S*-wave *inversion model* derived using the *seabed following initial model* is provided as Fig. S5.

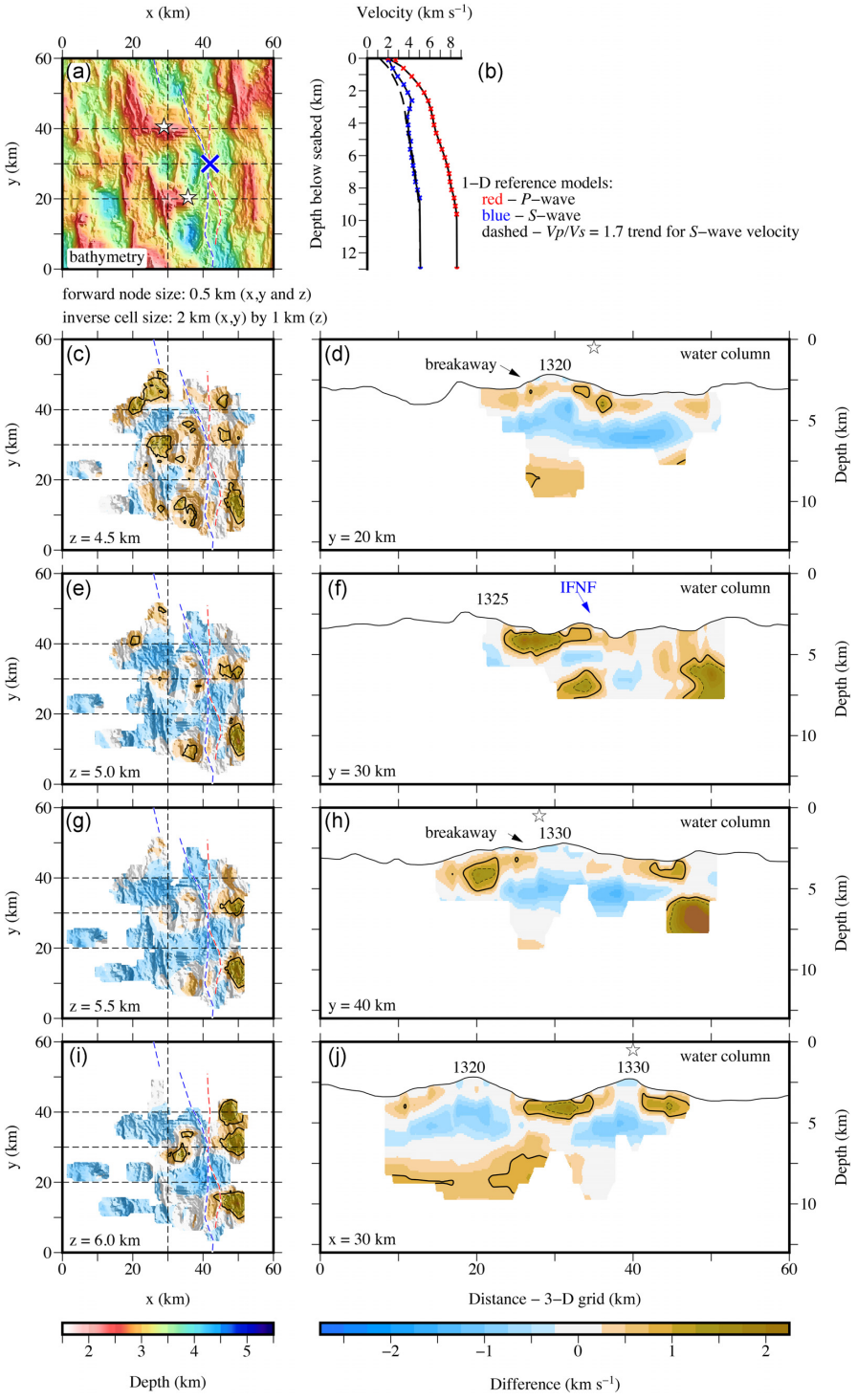

Figure 10. Slices through the 3-D grid plotted as the difference between the *S*-wave *inversion model* (Fig. 6), derived from the *sea surface parallel initial model* (Fig. 5), and a *reference model*. (a) Bathymetry map showing the proposed spreading centre from Mallows & Searle (2012—blue dashed line) and Simão *et al.* (2020—red dashed line), together with the location of active vent sites (white stars). Black dashed lines in (a) and in all horizontal (depth) slices indicate the locations of the vertical slices through the velocity model. (b) 1-D *P*-wave and *S*-wave *reference model* velocity–depth samples at $x = 42$ km, $y = 30$ km in the corresponding inversion models, location marked by the blue cross in (a), together with the conversion of the *P*-wave sample to *S*-wave using a *Vp*/*Vs* ratio of 1.7 (black dashed line) for comparison. This location was chosen as Simão *et al.* (2020) interpret it to lie where the crust is currently being formed by magma rich spreading. See text for details of *difference model* construction. (c) Depth slice through the *difference model* at $z = 4.5$ km bss. (d, f, h and j) Vertical slices through the *difference model* at the annotated model distances and with relevant features annotated. (e, g and i) Depth slices through the *difference model* at the annotated model depths bss. In all *difference model* parts, the +0.75 km s^{-1} (equivalent to Simão *et al.*'s 2020 +1.25 km s^{-1} *P*-wave difference contour—e.g. their fig. 7) and +1.25 km s^{-1} contours are annotated, and the slices are masked using the *inversion model* ray coverage. This approach to model representation clearly demonstrates (j) that the 1320 and 1330 OCCs are unlikely to be interconnected features along the same detachment. See Fig. 6 for details of each slice. An alternative version of this figure based on the 3-D *S*-wave *inversion model* derived using the *seabed following initial model* is provided as Fig. S6.

(>1.9) and magma rich formation (<1.9). This same proxy was modified by Peirce *et al.* (2019b) to 1.85, and later used by Peirce *et al.* (2020) to investigate the structure of the 13°N OCCs along the 2-D, north-south trending transect (Profile R). More widely, *Vp*/*Vs* and Poisson's ratio have been used to identify regions of increased hydration and serpentinization throughout the oceanic crust and mantle (*Vp*/*Vs* ratio of 1.8; $\sigma = 0.28$—Grevemeyer *et al.* 2018a), demonstrate the reduction of crustal porosity (σ decreasing by 0.0084 Myr^{-1}–Funnell *et al.* 2021), and investigate the closure of varying aspect ratio cracks throughout the oceanic crust as it ages (Spudich & Orcutt 1980; Shaw 1994; Christeson *et al.* 1997). To maintain consistency and enable comparison with other investigations of lithological variations at slower spreading centres, we primarily use the *Vp*/*Vs* ratio and set the magma poor/magma rich discriminator at 1.85, and note that such a value corresponds to $\sigma \approx 0.29$.

The *Vp*/*Vs* ratio varies significantly throughout the *Vp*/*Vs model* (Fig. 10). As with the *Vp* (Simão *et al.* 2020) and *Vs* models (Fig. 6), the most significant variation in the *Vp*/*Vs* ratio unsurprisingly occurs around and beneath the OCCs (Fig. 10), which are typically defined by higher values (>1.85) beneath the detachment surface, and lower values (<1.85) throughout the crust of the inter-OCC basin and current spreading centre. The higher *Vp*/*Vs* region (>1.85) beneath 1320 appears to extend over a greater lateral and vertical extent than that of 1330, although the *inversion model* is much less well constrained and has a lower resolution in the vicinity of 1330. At all crustal depths throughout the region to the west and east of 1320 and 1330, as well as between these and the further off-axis 1325, *Vp*/*Vs* is generally lower than 1.85, with the few regions >1.85 located in the parts of the model with lower resolution. This result is particularly significant for the inter-OCC basin that morphologically separates 1320 and 1330, as it suggests the crustal volume here is either or both lithologically and structurally distinct from the adjacent OCCs, and that it was magmatically accreted. A lack of model coverage further west prevents imaging the entire internal structure of the off-axis relic 1325, although Simão *et al.* (2020) find that it has a crustal *Vp* higher than at the spreading centre and lower than beneath the more ridge-proximal OCCs. The *Vp*/*Vs* ratio beneath the spreading centre (east of 40 km 3-D grid *x*-axis—Fig. 10; Mallows & Searle 2012; Simão *et al.* 2020) is consistently below 1.85 and, with the adjacent basin ($x = 30$ km, $y = 30$ km; Fig. 10a) having comparable values, suggests that these areas may be lithologically similar (magma rich) and even structurally related, that is magmatic accretion is currently ongoing at the spreading centre, at least between *ca*. $y = 25$–35 km, north–south.

5.3 Cross-plotting *Vp* and *Vs*

An alternative way to consider the variation in *Vp* and *Vs* in the context of lithology and morphology is to use a cross plot (Fig. 11). The *Vp*/*Vs* (and similarly Poisson's) ratio generally decreases with increasing distance (crustal age) from a spreading centre. Despite differences in experimental factors such as orientation relative to spreading direction, Spudich & Orcutt (1980), Au & Clowes (1984), Bratt & Solomon (1984) and Collier & Singh (1998) demonstrate this relationship for young crust (<15 Myr old—Fig. 11a), considering separately crust formed at spreading rates faster and slower than 35 mm yr^{-1} (average intermediate rate). In turn, Stephen *et al.* (1979), Shearer & Orcutt (1986), Duennebier *et al.* (1987), Bee & Bibee (1989) and Mithal & Mutter (1989) demonstrate this relationship for older crust (>50 Myr old—Fig. 11b). At the intermediate-spreading Costa Rica Rift, Funnell *et al.* (2021) consider the consistently decreasing *Vp*/*Vs* ratio in 0.25 Myr steps (Fig. 11d) along a 0–7 Ma transect running perpendicular to the spreading centre. Funnell *et al.* (2021) attribute the decrease with age to result primarily from a faster increase in *Vs* than *Vp*, and suggest that this results from thinner cracks being sealed and/or infilled preferentially over time (e.g. Shaw 1994; Christeson *et al.* 1997). It is also possible that the variation in *Vp*/*Vs* ratio is controlled by spreading rate (e.g. Grevemeyer *et al.* 2018a), with higher values representing a greater degree of alteration and serpentinization due to spreading being dominated by tectonism (Grevemeyer *et al.* 2018b—Fig. 11c), and lower values oceanic crust formed under predominantly magma rich conditions (e.g. White *et al.* 1992).

In Fig. 11(e), vertical samples through the *Vp/Vs model* at 1320, 1330 and at the mid-point in between in the inter-OCC basin, taken along 3-D grid $x = 30$ km (Figs 9a and j), are compared. Both 1320 and 1330 have *Vp/Vs*-depth profiles that consistently lie above Peirce *et al.*'s 2019a; 2019b) threshold of 1.85, while the inter-OCC basin more generally follows a trend of ∼1.7. This approach to *Vp*/*Vs model* understanding clearly supports the conclusion drawn from Simão *et al.*'s (2020) 3-D *P*-wave model, Peirce *et al.*'s (2019a) *P*-wave and density models and Peirce *et al.*'s (2020) *S*-wave model along the 2-D transect Profile R, and the 3-D *S*-wave modelling of this study, that both the 1320 and 1330 OCCs are composed primarily of highly altered rocks that originated in the lower crust and uppermost mantle. Also, the OCCs do not sit astride the same, single detachment surface running the length of the southern section of the 13°N segment (12°45′N to 13°45′N), since the crust that separates them from spreading centre to the toe of the relic 1325 OCC, now at ∼20 km off-axis to the west, formed by magma rich accretion.

6 DISCUSSION

Tomographic inversion of *S*-wave arrivals has generated a velocity model (Fig. 6) absent of vertical or lateral first-order velocity changes (i.e. velocity step or interface). While our *Vs inversion model* is consistent with that of the 2-D Profile R transect through the 1320 and 1330 OCCs (Peirce *et al.* 2020), given the complex local and regional geology and tectonic processes, we further discuss our results in the context of all available local data sets:

(i) Seafloor morphology, characteristics and geological sampling (MacLeod *et al.* 2009; Wilson *et al.* 2013; Bonnemains *et al.* 2017; Escartín *et al.* 2017; Searle *et al.* 2019).
(ii) Seismic tomography (Peirce *et al.* 2019a, 2020; Simão *et al.* 2020).
(iii) Gravity and magnetic potential field data (Mallows & Searle 2012; Searle *et al.* 2019; Peirce *et al.* 2019a).
(iv) Seismicity (Craig & Parnell-Turner 2017; Parnell-Turner *et al.* 2017, 2021).

Here, we use these data sets to discuss the likely structure and lithology (composition, porosity, permeability and temperature) of the OCCs along the 13°N segment at their various stages of evolution. We develop this understanding further to consider how OCC structure and lithology may be controlled by larger-scale tectonic processes and, finally, consider the possible drivers of known hydrothermal circulation systems.

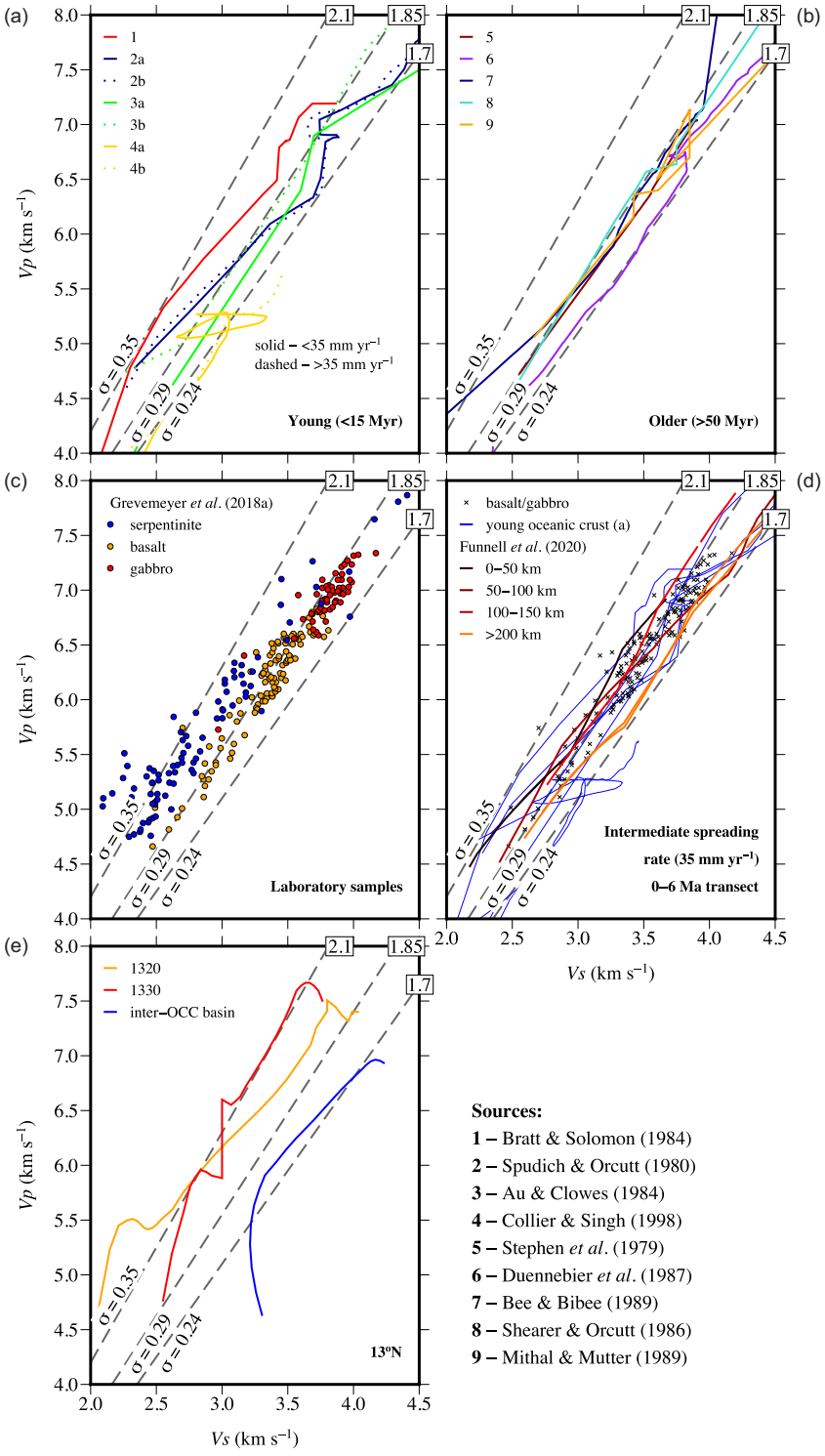

Figure 11. Summary of published 1-D *Vp/Vs* profiles, measurements from laboratory rock samples, and 1-D velocity–depth profiles taken along a 0–7 Ma flowline away from the Costa Rica Rift (Funnell *et al.* 2021). All plots show, as grey dashed lines, key *Vp/Vs* ratios annotated in boxes, and their equivalent Poisson's ratios. (a) 1-D *Vp/Vs* profiles from studies of young (<15 Myr old) oceanic crust, with numbers representing the references cited in the key. The solid lines represent centres spreading at <35mm yr^{-1}, and dashed >35mm yr^{-1}, which is the effective rate that Wilson *et al.* (2019) suggest defines whether magmatic or magma-dominated, faulting-enhanced spreading occurs. (b) Comparable profiles from studies of older (>50 Myr old) oceanic crust. (c) *Vp/Vs* relationship of laboratory samples from different oceanic crustal rocks (Grevemeyer *et al.* 2018a and references therein). (d) *Vp/Vs* relationship of 1-D velocity–depth profiles taken at different offsets away from the Costa Rica Rift (Funnell *et al.* 2021), superimposed on results from previous studies at young oceanic crustal sites (a), and mafic laboratory samples (b). (e) 1-D velocity–depth profiles taken through 1320, 1330 and the inter-OCC basin. Note how both the OCCs plot with a *Vp/Vs* ratio >1.85 throughout the entire crust, while the inter-OCC basin plots with a *Vp/Vs* ratio <1.85, suggesting that the latter formed under magma rich conditions and, thus, that the 1320 and 1330 OCCs are not interconnected along strike of the spreading centre, that is do not form part of the same detachment surface.

6.1 OCC lithology and structure

The *Vs inversion model* (Fig. 6), Simão *et al.*'s (2020) *Vp inversion model*, and the *Vp/Vs model* (Fig. 10) resulting from their combination, are all relatively smooth and artefact-free. Together, the high *Vp* (>5.5 km s^{-1}) and low *Vs* (<3.0 km s^{-1}) result in a high *Vp/Vs* ratio (>1.85) within the uppermost 3 km of the crust beneath both the 1320 and 1330 OCCs. Considering *Vp/Vs* solely as a seismically derived proxy for lithology and alteration, Grevemeyer *et al.* (2018a) proposed *Vp/Vs* > 1.9 to represent oceanic crust formed under magma poor conditions, whilst Peirce *et al.* 2019b, 2020) suggest that, based on *Vp/Vs* cross plots of mafic and serpentinized samples (e.g. Carlson & Miller 2003), *Vp/Vs* > 1.85 indicates the presence of serpentinized lithologies. In both proxies (Grevemeyer *et al.* 2018a; Peirce *et al.* 2019b, 2020), values below either threshold are taken to represent mafic oceanic crust formed under magma rich conditions. Following the Peirce *et al.* (2019b) proxy, which is applied along the 13°N segment of the MAR, the cores of both 1320 and 1330 OCCs are likely to be dominated by altered and/or serpentinized lithologies.

Evidence that the OCCs predominately comprise altered lower crust and uppermost mantle rocks is supported by dredging of the 1320 detachment surface, which recovered predominantly serpentinized peridotite and some gabbro (Fujiwara *et al.* 2003; MacLeod *et al.* 2009). Deeper sampling of other OCCs, from either faults that cut the detachment (MacLeod *et al.* 2002; Reston *et al.* 2002) or drilling (e.g. Dick *et al.* 2000; Kelemen *et al.* 2004; Blackman *et al.* 2006; Ildefonse *et al.* 2007), has recovered primarily gabbroic lithologies with serpentinization limited to the detachment surface. Crustal densities beneath the 1320, 1330 and 1348 detachment surfaces are modelled by Mallows & Searle (2012) to be 2900 ± 100 kg m^{-3} in the upper 2–5 km, while Peirce *et al.* (2019a) fit the observed free-air anomaly with densities between 2600 and 2900 kg m^{-3} within the footwall cut-off of the 1320 and 1330 OCCs and the Ashadze Complex (Fig. 1). In these cases, gravity modelling is unable to discriminate between gabbros and peridotites that are ∼50 per cent serpentinized (Mallows & Searle 2012).

Assuming, following Peirce *et al.* 2019b, 2020) and Grevemeyer *et al.* (2018a), that the high *Vp*/*Vs* ratio (>1.85; Fig. 11) is caused predominantly by alteration of peridotite, the low observed *Vs* (<3 km s^{-1}) requires the degree of serpentinization beneath the 1320 and 1330 OCCs to be >70 per cent, and would imply a lithological density of 2700–2800 kg m^{-3} (Miller & Christensen 1997). This density lies at the lower end of the range modelled previously (Mallows & Searle 2012; Peirce *et al.* 2019a), and suggests that a mechanism(s) in addition to serpentinization is required to achieve both the high modelled *Vp*/*Vs* ratio and moderate-to-low density. While this may simply be the presence of a mix of both gabbro and serpentinized peridotite (e.g. Reston 2018), crustal porosity with varying density, aspect ratio or crack orientation (e.g. Spudich & Orcutt 1980; Shaw 1994; Christeson *et al.* 1997) could also contribute significantly to the measured physical properties. Faulting and fractures are observed (e.g. Mallows & Searle 2012) and an expected consequence of the high degree of tectonic extension and flexure of the slower-spreading portions of this spreading system.

6.2 Faulting and tectonism

In Figs 12 and 13 we demonstrate how the variation in seismic velocity can be used to determine the generalized shape of detachment faults in the subsurface. Simão *et al.* (2020) use a +1.25 km s^{-1} *P*-wave velocity *difference model* contour to demarcate the detachment surface, in a similar manner to that adopted by deMartin *et al.* (2007). Here, we use the equivalent +0.75 km s^{-1} *S*-wave velocity *difference model* contour. Where model resolution is best (upper crust and beneath the 1320 OCC and inter-OCC basin), this contour is consistent with the location and dip of the shallower microseismicity (Parnell-Turner *et al.* 2017, 2021) on the southern side of 1320 (e.g. Fig. 12c), and clearly locates the inward-facing normal fault within the inter-OCC basin, and shows how it extends to depth through the upper crust (Fig. 12f). When compared to the reference point ($x = 42$ km, $y = 30$ km—Fig. 12h), the upper crust to the west of the spreading centre has an *S*-wave velocity higher than that at the ridge axis where magma rich accretion is postulated to be occurring (Simão *et al.* 2020). As this observation is consistent with the *P*-wave equivalent, it suggests that the cause is lithological rather than hydrothermal in origin.

The results of this study support the *local-scale* model of OCC development and evolution, and the implications that model has for faulting processes (MacLeod *et al.* 2009). The rapid thinning of the shallower crust across OCCs (Fig. 6j) reflects a disparity in tectonic heave between each OCC and the opposite flank of the spreading centre (MacLeod *et al.* 2009) that is not present elsewhere within the 13°N region. The thinning of the shallower crust across OCCs also coincides with locations of low backscatter terrain at the spreading centre, in contrast to the high backscatter volcanic terrain found throughout the rest of the region (Mallows & Searle 2012).

6.3 3-D perspective

A 3-D generalized perspective on OCC and detachment surface structure has been constructed using the +1.25 km s^{-1} difference contour in the case of the *P*-wave velocity–depth structure (Fig. 14) and the +0.75 km s^{-1} difference contour in the case of the *S*-wave velocity–depth structure (Fig. 15). Rotating movie views are also provided as Figs S10 & S11 respectively. The views, in particular the *P*-wave, also strongly suggest that the 1320 and 1330 OCCs do not form part of the same detachment surface, and are thus not connected beneath the inter-OCC basin. They also provide a means to consider the location and driving mechanism of the hydrothermal vent systems. As the positive difference contours are used, these constrain areas of higher velocity than at the spreading centre reference point, where the latter is also considered to represent oceanic crust formed during magma rich (or magma-dominated) conditions. In the case of the *P*-wave 3-D model this most likely represents exhumed rocks of the lower crust and uppermost mantle, altered or otherwise, which should have a velocity and density higher than that of the basalts expected of the upper-to-mid crust. Such rocks should also have a higher *S*-wave velocity, unless extensively altered, heated, highly fractured or containing significant high permeability pathways filled with circulating hydrothermal fluid.

Several hydrothermal fields have been found within the 13°N segment, including on the exposed 1320 and 1330 detachment surfaces (Fig. 1; e.g. Beltenev *et al.* 2007; Cherkashov *et al.* 2010b; Pertsev *et al.* 2012; Bortnikov *et al.* 2015). The 1330 vents are up to ∼100 kyr in age and show no apparent age versus distance off-axis correlation. Older deposits from extinct systems are found near the axis while, in contrast, active sites are found more than 5 km off-axis (Cherkashov *et al.* 2010a), implying multiple circulation driving mechanisms operate, including off-axis heat sources, such as magma intrusions within the footwall, and fluids percolating

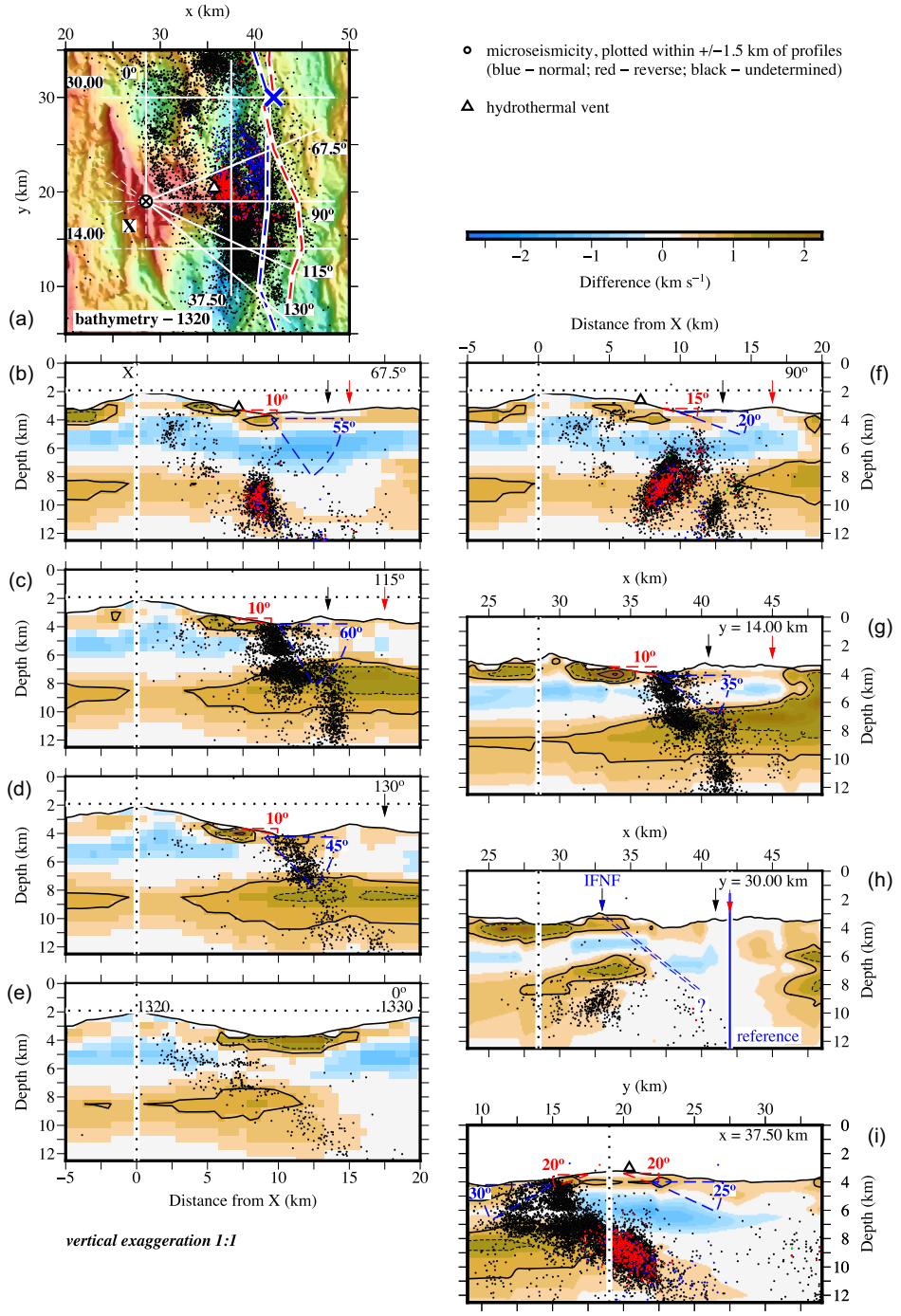

Figure 12. 1320 OCC detachment geometry from slices through the 3-D grid plotted as the difference between the *S*-wave *inversion model* (Fig. 6), derived from the *sea surface parallel initial model* (Fig. 5), and a *reference model* (after Simão *et al.* 2020). a) Bathymetry surrounding the 1320 OCC with microseismic events (Parnell-Turner *et al.* 2017) coloured according to mechanism (see legend). White lines locate cross-sections shown in (b–i) with azimuths or *x*,*y* coordinates annotated in black. White triangle marks the Irinovskoe vent site in all relevant parts and the circled cross the intersection of each cross-section at the OCC (vertical dotted line in all other parts). Red dashed line marks the trend of the proposed spreading centre location based on the crustal structure derived from Simão *et al.*'s (2020) *P*-wave *inversion model*. Mallows & Searle's (2012) average spreading centre is marked by the blue dashed line. Blue cross shows the 1-D reference profile location. (b)–(i) Vertical cross-sections through the *difference model* at various azimuths, with earthquake hypocentres annotated. Sections are annotated in the top right corners by their azimuths (b–f) or are annotated by their *x* or *y* coordinate (g–i). Red arrows locate Simão *et al.*'s (2020) proposed spreading centre further to the east, based on crustal velocity–depth structure; black arrows indicate the average spreading centre of Mallows & Searle (2012). Red and blue dashed wedges indicate the changing dip (annotated) of the detachment fault plane, based on the +1.25 km s^{-1} velocity difference contour of Simão *et al.*'s (2020) *P*-wave *inversion model*, on the exposed surface and at depth. Horizontal dotted line marks the shallowest depth of the 1320 OCC. IFNF—inward-facing normal fault. In all *difference model* parts, the +0.75 km s^{-1} (equivalent to Simão *et al.*'s 2020 +1.25 km s^{-1} *P*-wave difference contour—e.g. their fig. 7) and +1.25 km s^{-1} contours are annotated. An alternative version of this figure based on the 3-D *S*-wave *inversion model* derived using the *seabed following initial model* is provided as Fig. S7.

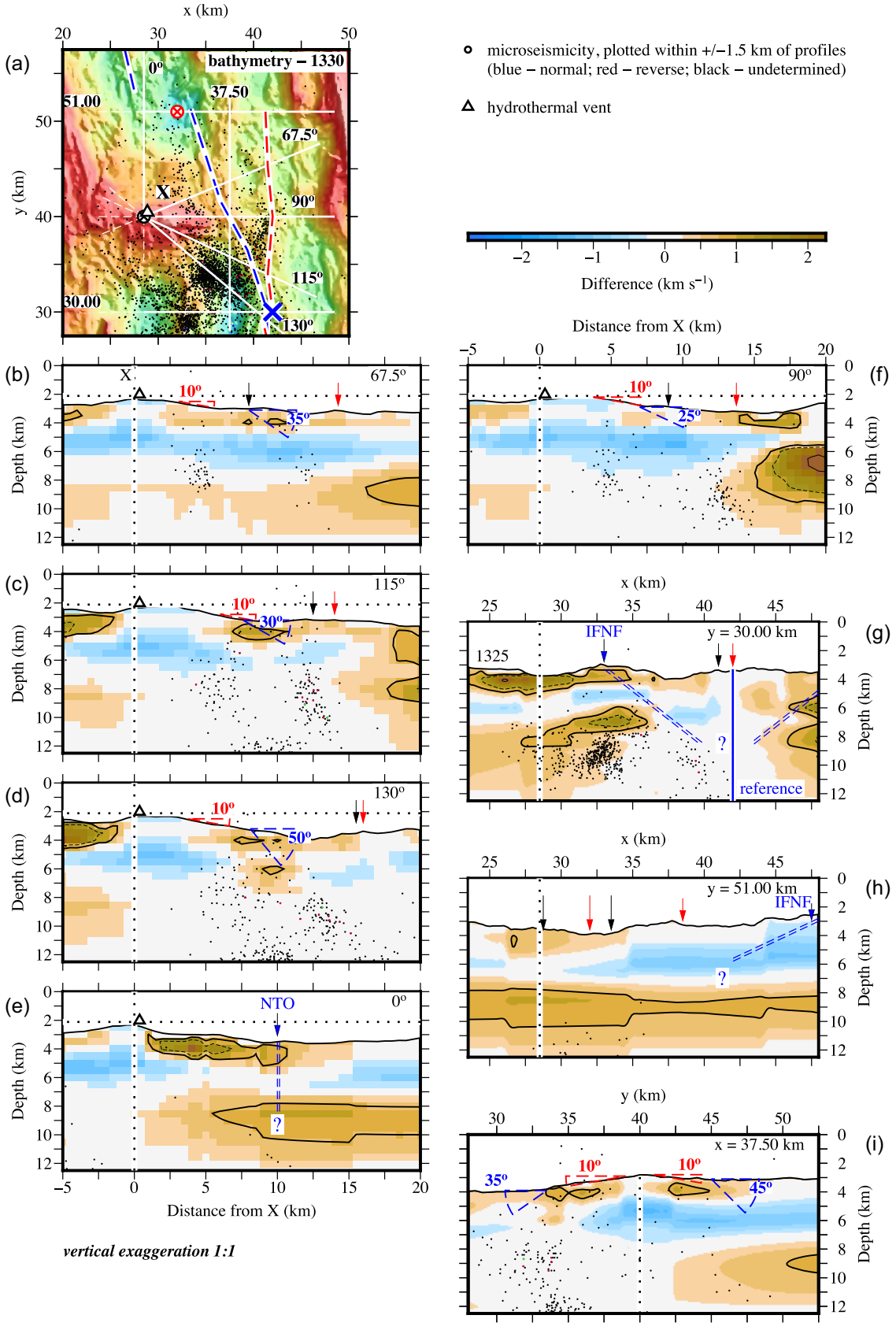

Figure 13. 1330 OCC detachment geometry. See Fig. 12 for details. The red circled cross in (a) marks the general location of the non-transform offset (NTO) shown in (e). White triangle marks the Semyenov vent site in all relevant parts. An alternative version of this figure based on the 3-D *S*-wave *inversion model* derived using the *seabed following initial model* is provided as Fig. S8.

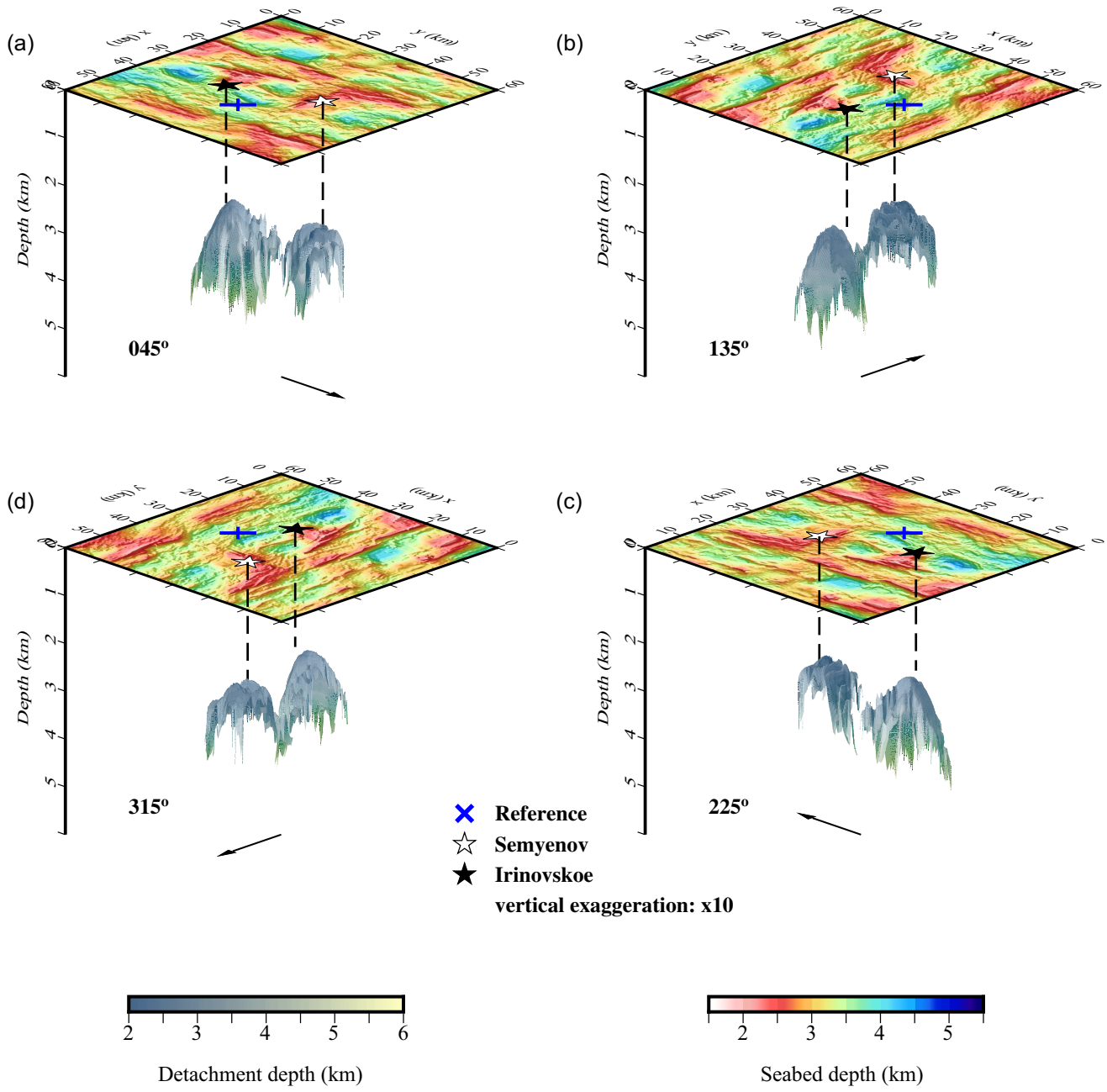

Figure 14. 3-D perspective view of the generalized shape of the 1320 and 1330 OCC detachment surfaces based on the +1.25 km s^{-1} contour from Simão *et al.*'s (2020) *P*-wave *difference model*, viewed from an azimuth of (a) 045°, (b) 135°, (c) 225° and (d) 315°. The location of the reference point (blue cross) and the Semyenov (white star) and Irinovskoe (black star) are shown on the bathymetry plotted above each 3-D view, extended to their seabed depths by the black dashed lines. Black arrow points north. A rotating movie version of this figure is provided as Fig. S10.

along the detachment surface sub-seabed even after it reaches the end of its active life span.

The two active vent fields, Irinovskoe and Semyenov (Fig. 1), are located in different settings on the 1320 and 1330 OCCs, respectively. Irinovskoe lies on the active 1320 detachment surface adjacent to its spreading centre-proximal toe (otherwise known as the hanging-wall cut-off), while Semyenov lies westwards of the breakaway (seabed footwall cut-off of the detachment) of the 1330 detachment that is thought to now be in the final stages of its life cycle or recently inactive. In both cases, the seismic velocity models (Simão *et al.* 2020; Figs 5b & 6) show that there is no apparent velocity anomaly (within model resolution constraints) underlying each vent site. In the case of the *P*-wave model, 2 × 2 × 1 km-sized anomalies with velocity perturbations as low as 5 per cent of the surrounding crust should be well resolved. Thus, if a heat source for Irinovskoe vent site is situated immediately beneath it, it is quite spatially restricted and/or limited in thermal/velocity contrast to its surrounds. Analogous observations can be made for the 1330 OCC where the source for the Semyenov vent site would have to be smaller than 3 × 3 × 1 km if situated in the shallower part of the OCC and smaller than 5 × 5 × 1 km if at mid-crustal depth.

The corresponding *S*-wave model and the observed traveltime picks on which it is based, even though the resolution is poorer, may go some way towards explaining the differences in characteristics

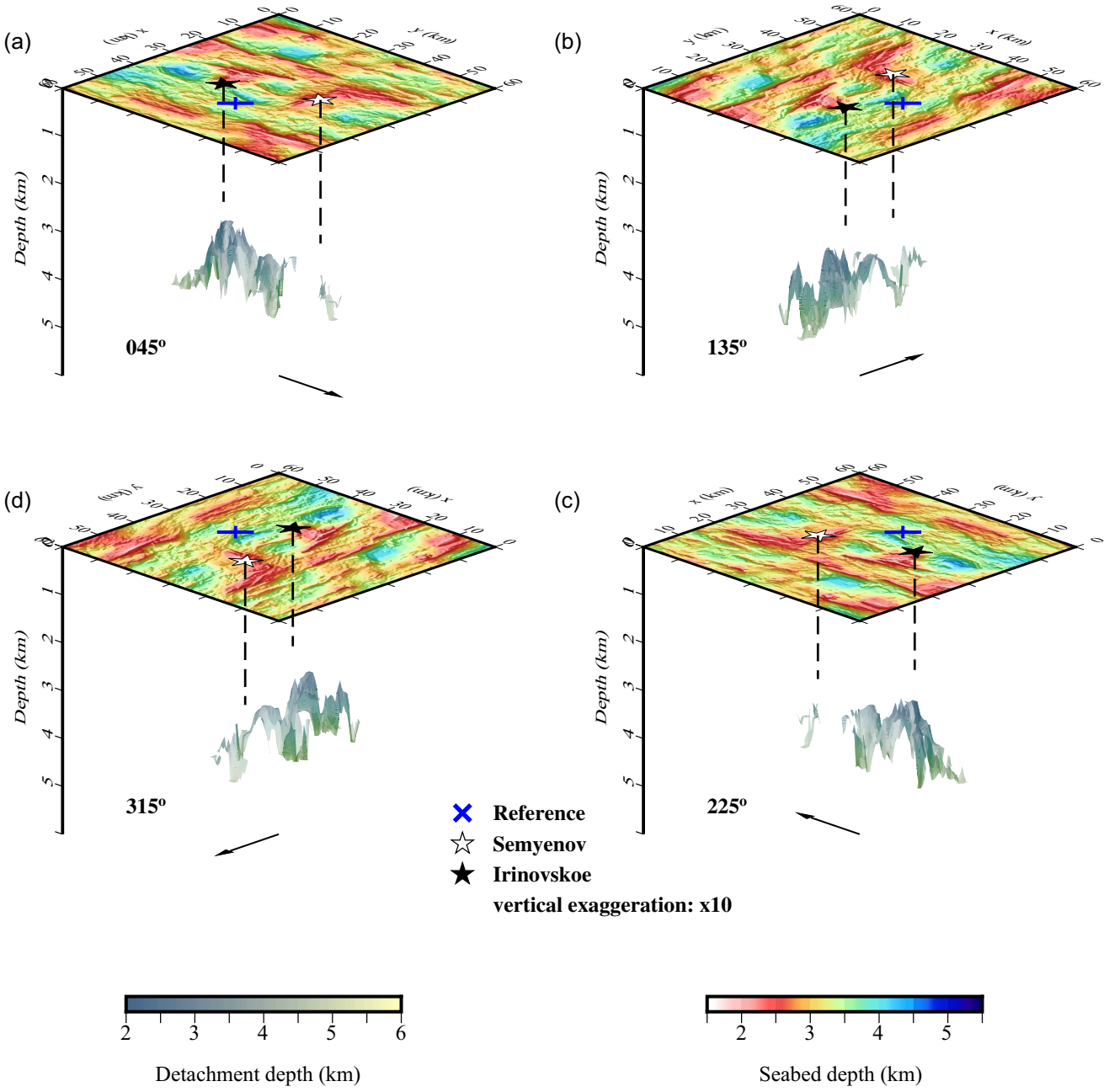

Figure 15. 3-D perspective view of the generalized shape of the 1320 and 1330 OCC detachment surfaces based on the + 0.75 km s^{-1} contour from the *S*-wave *difference model* (Fig. 6) derived using the *sea surface parallel initial model* (Fig. 5), viewed from an azimuth of (a) 045°, (b) 135°, (c) 225° and (d) 315°. The location of the reference point (blue cross) and the Semyenov (white star) and Irinovskoe (black star) are shown on the bathymetry plotted above each 3-D view, extended to their seabed depths by the black dashed lines. Black arrow points north. A rotating movie version of this figure is provided as Fig. S11.

of these contrasting vent sites. Although covered by an equivalent density of OBSs and shooting profiles, fewer *S*-wave arrivals are observed for shots fired over, and surrounding, the 1330 OCC. Although this could arise simply as a consequence of the rugged topography affecting instrument-seabed coupling, although the same argument could be made for 1320, it could equally be caused by the crustal material subseabed being hotter, or being intruded by partially molten pluton(s), and, thus, attenuating of propagating *S*-waves. In such a case, it might be expected that the *S*-wave velocity would be lower than anticipated for exhumed lower crustal and upper mantle material, and more equivalent to that at the spreading centre (the reference point) where magma rich accretion is currently thought to dominate. Consequently, fluid circulation at Semyenov at 1330 may be driven by magmatic intrusion into the footwall, while that at Irinovskoe at 1320 may take advantage of open pervasive permeability (fractures and faults) within the footwall (e.g. due to its roll-over to a shallower angle) and a thermal gradient sustained by the adjacent spreading centre.

7 CONCLUSIONS

We have modelled the 3-D *S*-wave seismic velocity–depth structure within the OCC-dominated 13°N segment of the MAR to test the relationship between adjacent OCCs and explore the likely lithologies

that comprise these widespread, yet enigmatic, features. Limited observations of *S*-wave arrivals within the OBS record sections result in a corresponding traveltime pick data set with 20-times fewer shot-receiver pick pairs than for the coincident *P*-wave experiment presented by Simão *et al.* (2020). This much reduced sampling results in model constraint limited to the 1320 OCC and the inter-OCC basin primarily, with features resolved at a scale equivalent to average along axis extent of an OCC. We draw the following conclusions:

(i) The *Vs inversion model* resolves regions of relatively low *Vs* (<3 km s^{-1}) beneath the 1320 and 1330 detachments, and higher *Vs* (>3 km s^{-1}) in the inter-OCC basin and regions surrounding the detachments.

(ii) Combination of our *Vs inversion model* with the *LRDM* (*Vp*) *inversion model* of Simão *et al.* (2020), results in a unique 3-D *Vp/Vs model* that indicates the prevalence of a relatively high *Vp/Vs* ratio associated with OCCs and lower values, more typical of oceanic crust formed under magma rich conditions, in the surrounding areas.

(iii) High *Vp/Vs* ratio within the OCCs suggests the crust formed by tectonic processes and, based on previous density modelling (Peirce *et al.* 2019a, 2020), reflects either pervasive serpentinization, highly faulted and fractured gabbroic lithologies, or a combination of the two.

(iv) Based on the *Vp/Vs model* showing the intervening crust to be equivalent of that at the magma rich adjacent spreading centre, from seabed to lower crust, our 3-D grid tomographic results support the *local-scale* hypothesis (MacLeod *et al.* 2009) in which OCCs are associated with independent detachment faults. Although it could be argued that the detachment may undulate laterally in the along axis direction, this would need to be more than 3 km in amplitude to be consistent with observations and modelling results.

(v) Our *Vs inversion model* suggests that the 1320 and 1330 vent fields have different hydrothermal circulation drivers, with the 1330 field driven by magma intrusions and the 1320 field driven by the spreading centre thermal gradient and pervasive flow along open permeability.

ACKNOWLEDGMENTS

This research project was funded by the NERC Natural Environment Research Council (NERC) grant NE/J02029X/1, NE/J022551/1 and NE/J021741/1. We would like to thank all those involved in the planning and acquisition of data during research cruise JC132 (Reston & Peirce 2016), including the officers, engineers and crew of the RRS James Cook, the scientific party, and all seagoing NERC facility technicians and engineers. The NERC Ocean-Bottom Instrumentation Facility (Minshull *et al.* 2005) provided the OBSs and their technical support at sea. Seismic data were processed and manipulated for plotting using Seismic Unix (Cohen & Stockwell 2010). All figures were prepared using the Generic Mapping Tools (GMT) package (Wessel *et al.* 2013). The final accepted version of this manuscript is available through Durham Research Online (dro.dur.ac.uk). We thank Gaye Bayrakci and an anonymous reviewer for their positive and helpful comments.

DATA AVAILABILITY

Data from cruises JC102, JC109 and JC132 are archived at the NERC's British Oceanographic Data Centre and are available from the following links:

JC102–www.bodc.ac.uk/resources/inventories/cruise_inventory/report/15024/,

JC109–www.bodc.ac.uk/resources/inventories/cruise_inventory/report/15031/ and

JC132–www.bodc.ac.uk/resources/inventories/cruise_inventory/report/16046/.

REFERENCES

Au, D. & Clowes, R.M., 1984. Shear-wave velocity structure of the oceanic lithosphere from ocean bottom seismometer studies, *Geophys. J. R. astr. Soc.,* **77**(1), 105–123.

Batista, L., Hübscher, C., Terrinha, P., Matias, L., Afilhado, A. & Lüdmann, T., 2017. Crustal structure of the Eurasia–Africa plate boundary across the Gloria Fault, North Atlantic Ocean, *Geophys. J. Int.,* **209**(2), 713–729.

Bee, M. & Bibee, L.D., 1989. A seismic refraction study of Cretaceous oceanic lithosphere in the northwest Pacific basin, *Mar. Geophys. Res.,* **11**(4), 239–261.

Beltenev, V. *et al.*, 2007. A new hydrothermal field at 13°30 N on the Mid-Atlantic Ridge, *InterRidge News,* **16,** 10–11.

Bergman, E.A. & Solomon, S.C., 1980. Oceanic intraplate earthquakes – implications for local and regional intraplate stress, *J. geophys. Res.,* **85,** 5389–5410.

Bergman, E.A. & Solomon, S.C., 1990. Earthquake swarms on the Mid-Atlantic Ridge: products of magmatism or extensional tectonics?, *J. geophys. Res.,* **95,** 4943–4965.

Blackman, D.K., Abe, N., Carlson, R.L., Guerin, G., Ildefonse, B. & Kumpf, A., 2019. Seismic properties of gabbroic sections in oceanic core complexes: constraints from seafloor drilling, *Mar. Geophys. Res.,* **40**(4), 557–569.

Blackman, D.K., Canales, J.-P. & Harding, A., 2009. Geophysical signatures of oceanic core complexes, *Geophys. J. Int.,* **178**(2), 593–613.

Blackman, D.K., Cann, J.R., Janssen, B. & Smith, D.K., 1998. Origin of extensional core complexes: evidence from the Mid-Atlantic Ridge at Atlantis Fracture Zone, *J. geophys. Res.,* **103,** 21 315–21 333.

Blackman, D.K., Ildefonse, B., John, B.E., Ohara, Y., Miller, D.J. & MacLeod, C.J. 2006. Expedition 304/305 Scientists, in *Proceedings of the Integrated Ocean Drilling Program,* Integrated Drilling Program Management International Inc.,College Station, TX.

Blackman, D.K., Karner, G.D. & Searle, R.C., 2008.Three-dimensinal structure of oceanic core complexes: effects on gravity signature and ridge flank morphology, Mid-Atlantic Ridge, 30° N, *Geochem. Geophys. Geosyst.,* **9**(6), doi:10.1029/2008GC001951.

Blackman, D.K. *et al.*, 2002. Geology of the Atlantis Massif (Mid-Atlantic Ridge, 30° N): implications for the evolution of an ultramafic oceanic core complex, *Mar. Geophys. Res.,* **23**(5-6), 443–469.

Bonnemains, D., Escartín, J., Mével, C. & Andreani, M., 2017. Pervasive silicification and hanging wall overplating along the 13°20′N oceanic detachment fault (Mid-Atlantic Ridge), *Geochem. Geophys. Geosyst.,* **18,** 2028–2053.

Bortnikov, N.S., Simonov, V.A., Borovikov, A.A., Bel'tenev, V.E., Amplieva, E., Kotlyarov, A.V. & Bryanskiy, N.V., 2015. The metalliferous fluid of the hydrothermal sulfide system associated with the oceanic core complex 13°20N: the Mid-Atlantic Ridge (LA-ICP-MS and fluid inclusions), in *Proceedings of the Oceanic Core Complexes and Hydrothermalism, Russian Ridge 2015 Workshop Program,* Moscow, Russia, pp. 80–83.

Bratt, S.R. & Solomon, S.C., 1984. Compressional and shear-wave structure of the East Pacific Rise at 11°20'N – constraints from 3-component ocean bottom seismometer data, *J. geophys. Res.,* **89,** 6095–6110.

Buck, W.R., 1988. Flexural rotation of normal faults, *Tectonics,* **7,** 959–973.

Buck, W.R., Lavier, L.L. & Poliakov, A.N.B., 2005. Modes of faulting at mid-ocean ridges, *Nature,* **434,** 719–723.

Canales, J.P., Sohn, R.A. & deMartin, B.J., 2007. Crustal structure of the Trans-Atlantic Geotraverse (TAG) segment (Mid-Atlantic Ridge, 26°10'N): implications for the nature of hydrothermal circulation and detachment faulting at slow spreading ridges, *Geochem. Geophys. Geosyst.,* **8**(8), doi:10.1029/2007GC001629.

Canales, J.P., Tucholke, B.E. & Collins, J.A., 2004. Seismic reflection imaging of an oceanic detachment fault: Atlantis Megamullion (Mid-Atlantic Ridge, 30°10'N), *Earth planet. Sci. Lett.,* **222,** 543–560.

Canales, J.P. *et al.*, 2008. Seismic evidence for large-scale compositional heterogeneity of oceanic core complexes, *Geochem. Geophys. Geosyst.,* **9**(8),.

Cann, J.R. *et al.*, 1997. Corrugated slip surfaces formed at ridge-transform intersections on the Mid-Atlantic Ridge, *Nature,* **385,** 329–332.

Cannat, M., 1993. Emplacement of mantle rocks in the seafloor at mid-ocean ridges, *J. geophys. Res.,* **98,** 4163–4172.

Carlson, R.L. & Miller, D.J., 2003. Mantle wedge water contents estimated from seismic velocities in partially serpentinized periodotites. *Geophys. Res. Letts.,* **30**(5), doi:10.1029/2002GL016600.

Cherkashov, G., Lazareva, L. & Stepanova, T., 2010a. Massive sulfide deposits at Semyenov cluster: mineralogy, age and evolution, in *Proceedings of the Joint International Meeting Miner. Ocean Deep Miner. Min.,* St. Petersburg, Russia, pp. 52–57.

Cherkashov, G. *et al.*, 2010b. Seafloor massive sulfides from the northern equatorial Mid-Atlantic Ridge: new discoveries and perspectives, *Mar. Georesour. Geotechnol.,* **28**(3), 222–239.

Christensen, N.I., 1996. Poisson's ratio and crustal seismology, *J. geophys. Res.,* **101**(B2), 3139–3156.

Christeson, G.L., Shaw, P.R. & Garmany, J.D., 1997. Shear and compressional wave structure of the East Pacific Rise, 9°10'N, *J. geophys. Res.,* **10**(B4), 7821–7835.

Cohen, J.K. & Stockwell, J.W., 2010. CWP/SU: seismic Un∗x Release No. 42: an open source software package for seismic research and processing, Center for Wave Phenomena, Colorado School of Mines.

Collier, J.S. & Singh, S.C., 1998. Poisson's ratio structure of young oceanic crust, *J. geophys. Res.,* **103**(B9), 20 981–20 996.

Collins, J.A., Blackman, D.K., Harris, A. & Carlson, R.L., 2009. Seismic and drilling constraints on velocity structure and reflectivity near IODP hole U1309D on the central dome of Atlantis Massif, Mid-Atlantic Ridge 30° N, *Geochem. Geophys. Geosyst.,* **10**(1), doi:10.1029/2008GC002121.

Craig, T.J. & Parnell-Turner, R., 2017. Depth-varying seismogenesis on an oceanic detachment fault at 13°20′N on the Mid-Atlantic Ridge, *Earth planet. Sci. Lett.,* **479,** 60–70.

deMartin, B.J., Sohn, R.A., Canales, J.P. & Humphris, S.E., 2007. Kinematics and geometry of active detachment faulting beneath the Trans-Atlantic Geotraverse (TAG) hydrothermal vent field on the Mid-Atlantic Ridge, *Geology,* **35,** 711–714.

Dick, H.J.B., Lin, J. & Schouten, H., 2003. An ultraslow-spreading class of ocean ridge, *Nature,* **426,** 405–412.

Dick, H.J.B. *et al.*, 2000. A long in-situ section of the lower ocean crust: results of ODP Leg 176 drilling at Southwest Indian Ridge, *Earth planet. Sci. Lett.,* **179,** 31–51.

Duennebier, F.K., Anderson, P.N. & Fryer, G.J., 1987. Azimuth determination of and from horizontal ocean bottom seismic sensors, *J. geophys. Res.,* **92**(B5), 3567–3572.

Escartín, J. & Canales, J.P., 2011. Detachments in oceanic lithosphere: deformation, magmatism, fluid flow, and ecosystems, *EOS, Trans. Am. Geophys. Un.,* **92**(4), 31–32.

Escartín, J., Hirth, G. & Evans, B., 1997. Effects of serpentinization on the lithospheric strength and the style of normal faulting at slow-spreading ridges, *Earth planet. Sci. Lett.,* **151,** 181–189.

Escartín, J., Smith, D. & Cannat, M., 2003b. Parallel bands of seismicity at the Mid-Atlantic Ridge, 12–14° N, *Geophys. Res. Lett.,* **30**(12),.

Escartín, J., Cowie, P.A., Searle, R.C., Allerton, S., Mitchell, N.C., MacLeod, C.J. & Slootweg, A.P., 1999. Quantifying tectonic strain and magmatic accretion at a slow spreading ridge segment, Mid-Atlantic Ridge, 29° N, *J. geophys. Res.,* **104**(B5), 10 421–10 437.

Escartín, J., Mével, C., MacLeod, C.J. & McCaig, A.M., 2003a. Constraints on deformation conditions and the origin of oceanic detachments: the Mid-Atlantic Ridge core complex at 15°45′ N, *Geochem. Geophys. Geosyst.,* **4**(8),.

Escartín, J., Smith, D.K., Cann, J., Schouten, H., Langmuir, C.H. & Escrig, S., 2008. Central role of detachment faults in accretion of slow-spreading oceanic lithosphere, *Nature,* **455,** 790–794.

Escartín, J. *et al.*, 2017. Tectonic structure, evolution, and the nature of oceanic core complexes and their detachment fault zones (13°20'N and 13°30'N, Mid-Atlantic Ridge), *Geochem. Geophys. Geosyst.,* **18,** 1451–1482.

Fujiwara, T., Lin, J., Matsumoto, T., Kelemen, P.B., Tucholke, B.E. & Casey, J.F., 2003. Crustal evolution of the Mid-Atlantic Ridge near the Fifteen-Twenty Fracture Zone in the last 5 Ma, *Geochem. Geophys. Geosyst.,* **4**(3), doi:10.1029/2002GC000364.

Funnell, M.J., Robinson, A.H., Hobbs, R.W. & Peirce, C., 2021. Evolution and properties of young oceanic crust: constraints from Poisson's ratio. *Geophys. J. Int.,* **225**(3), 1874–1896.

Grevemeyer, I., Ranero, C.R. & Ivandic, M., 2018a. Structure of oceanic crust and serpentinization at subduction trenches, *Geosphere,* **14**(2), 395–418.

Grevemeyer, I., Reston, T.J. & Moeller, S., 2013. Microseismicity of the Mid-Atlantic Ridge at 7°S-8°15′S and at the Logatchev Massif oceanic core complex at 14°40′N-14°50′N, *Geochem. Geophys. Geosyst.,* **14,** 3532–3554.

Grevemeyer, I., Hayman, N.W., Peirce, C., Schwardt, M., Van Avendonk, H.J.A. & Dannowski, A., 2018b. Episodic magmatism and serpentinized mantle exhumation at an ultraslow-spreading centre, *Nature,* **11,** 444–448.

Grevemeyer, I., Rüpke, L.H., Morgan, J.P., Iyer, K. & Devey, C.W., 2021. Extensional tectonics and two-stage crustal accretion at oceanic transform faults. *Nature,* **591,** 402–407.

Harding, J.L., Van Arendonk, H.J.A., Hayman, N.W., Grevemeyer, I. & Peirce, C., 2017. Magmatic-tectonic conditions for hydrothermal venting on an ultraslow-spread oceanic core complex. *Geology,* **45,** 839–842.

Hensen, C. *et al.,* 2019. Marine transform faults and fracture zones: a joint perspective integrating seismicity, fluid flow and life. *Front. Earth Sci.,* **7,** 39.

Howell, S.M. *et al.*, 2019. Seafloor expression of oceanic detachment faulting reflects gradients in mid-ocean ridge magma supply, *Earth planet. Sci. Lett.,* **516,** 176–189.

Ildefonse, B., Blackman, D.K., John, B.E., Ohara, Y., Miller, D.J. & MacLeod, C.J. Integrated Ocean Drilling Program Expeditions 304/305 Science Party, 2007. Oceanic core complexes and crustal accretion at slow-spreading ridges, *Geology,* **35**(7), 623–626.

Kelemen, P.B., Kikawa, E. & Miller, J., 2004. Igneous crystallization and localized deformation >15 km beneath the Mid-Atlantic Ridge, 14-16 N, *Geochem. Cosmo. Acta,* **68**(11), A690.

MacLeod, C.J. *et al.*, 2002. Direct geological evidence for oceanic detachment faulting: the Mid-Atlantic Ridge, 15°45′N, *Geology,* **30,** 879–882.

MacLeod, C.J. *et al.*, 2009. Life cycle of oceanic core complexes, *Earth planet. Sci. Lett.,* **287,** 333–344.

Mallows, C. & Searle, R.C., 2012. A geophysical study of oceanic core complexes and surrounding terrain, Mid-Atlantic Ridge 13°N–14°N, *Geochem. Geophys. Geosyst.,* **13**(6), doi:10.1029/2012GC004075.

Miller, D.J. & Christensen, N.I., 1997. Seismic velocities of lower crustal and upper mantle rocks from the slow-spreading Mid-Atlantic Ridge, south of the Kane Transform Zone (MARK), *Proc. Ocean Drill. Program Sci. Results,* **153,** 437–454.

Minshull, T.A., Sinha, M.C. & Peirce, C., 2005. Multi-disciplinary subseabed geophysical imaging - a new pool of 28 seafloor instruments in use by the United Kingdom Ocean Bottom Instrument Consortium, *Sea Technol.*, **46,** 27–31.

Mithal, R. & Mutter, J.C., 1989. A low-velocity zone within the layer 3 region of 118-Myr old oceanic-crust in the western North Atlantic, *Geophys. J. R. astr Soc.,* **97**(1), 275–294.

Muller, R.D., Sdrolias, M., Gaina, C. & Roest, W.R., 2008. Age, spreading rates, and spreading asymmetry of the world's ocean crust, *Geochem. Geophys. Geosyst.,* **9**(4), doi:10.1029/2007GC001743.

Nooner, S.L., Sasagawa, G.S., Blackman, D.K. & Zumberge, M.A., 2003. Structure of oceanic core complexes: constraints from seafloor gravity measurements made at the Atlantis Massif, *Geophys. Res. Lett.,* **30**(8), doi:10.1029/2003GL017126.

Olive, J.-A., Parnell-Turner, R., Escartín, J., Smith, D.K. & Petersen, S., 2019. Controls on the seafloor exposure of detachment fault surfaces, *Earth planet. Sci. Lett.,* **506,** 381–387.

Parnell-Turner, R., Sohn, R.A., Peirce, C., Reston, T.J., MacLeod, C.J., Searle, R.C. & Simão, N., 2017. Oceanic detachment faults generate compression in extension, *Geology,* **45,** 923–926.

Parnell-Turner, R., Sohn, R.A., Peirce, C., Reston, T.J., MacLeod, C.J., Searle, R.C. & Simão, N.M., 2021. Seismicity trends and detachment fault structure at 13°N, Mid-Atlantic Ridge. *Geology,* **49**(3), 320–324.

Peirce, C., 2014a. The role and detachment of faulting at slow-spreading mid-ocean ridges, RRS James Cook cruise report JC102, Durham University (unpublished), pp. 19, https://www.bodc.ac.uk/resources/inventories/cruise_ inventory/reports/jc102.pdf.

Peirce, C., 2014b. The role and detachment of faulting at slow-spreading mid-ocean ridges, RRS James Cook Cruise Report JC109, Durham University (unpublished), pp. 26, https://www.bodc.ac.uk/resources/inventories/cruise_ inventory/reports/jc109.pdf.

Peirce, C. & Day, A.J., 2002. Ocean-bottom seismograph tomographic experiments- a consideration of acquisition geometries vs. resources, *Geophys. J. Int.,* **151**(2), 543–566.

Peirce, C., Reveley, G., Robinson, A.H., Funnell, M.J., Searle, R.C., Simão, N.M., MacLeod, C.J. & Reston, T.J., 2019a. Constraints on crustal structure of adjacent OCCs and segment boundaries at 13°N on the Mid-Atlantic Ridge, *Geophys. J. Int.,* **217**(2), 988–1010.

Peirce, C., Robinson, A.H., Campbell, A.M., Funnell, M.J., Grevemeyer, I., Hayman, N.W., Van Avendonk, H.J.A. & Castiello, G., 2019b. Seismic investigation of an active ocean-continent transform margin: the interaction between the Swan Islands Fault Zone and the ultraslow-spreading Mid-Cayman Spreading Centre, *Geophys. J. Int.,* **219**(1), 159–184.

Peirce, C., Robinson, A.H., Funnell, M.J., Searle, R.C., MacLeod, C.J. & Reston, T.J., 2020. Magmatism versus serpentinization - crustal structure along the 13°N segment at the Mid-Atlantic Ridge, *Geophys. J. Int.,* **221**(2), 981–1001.

Pertsev, A.N., Bortnikov, N.S., Vlasov, E.A., Beltenev, V.E., Dobretsova, I.G. & Ageeva, O.A., 2012. Recent massive sulphide deposits of the Semenov ore district, Mid-Atlantic Ridge, 1331N: associated rocks of the oceanic core complex and their hydrothermal alteration, *Geol. Ore Deposits,* **54,** 334–346.

Reston, T.J., 2018. Flipping detachments: the kinematics of ultraslow spreading ridges, *Earth planet. Sci. Lett.,* **503,** 133–157.

Reston, T. & Peirce, C., 2016. The role and detachment of faulting at slow-spreading mid-ocean ridges, RRS James Cook Cruise Report JC132, Durham University (unpublished), pp. 62, https://www.bodc.ac.uk/resources/inventories/cruise inventory/reports/jc132.pdf.

Reston, T.J. & Ranero, C.R., 2011. The 3-D geometry of detachment faulting at mid-ocean ridges, *Geochem. Geophys. Geosyst.,* **12**(7), 10.1029/2011GC003666.

Reston, T., Weinrebe, W., Grevemeyer, I., Flueh, E.R., Mitchell, N.C., Kirstein, L., Kopp, C. & Hopp, H. participants of Meteor 47/2, 2002. A rifted inside corner massif on the Mid-Atlantic Ridge at 5°S, *Earth planet. Sci. Lett.,* **200,** 255–269.

Sandiford, D., Brune, S., Glerum, A., Naliboff, J. & Whittaker, J.M., 2021. Kinematics of footwall exhumation at detachment faults: solid-block rotation and apparent unbending, *Geochem., Geophys., Geosys,* **22**(4),.

Sauter, D. *et al.*, 2013. Continuous exhumation of mantle-derived rocks at the Southwest Indian Ridge for 11 million years, *Nat. Geosci.,* **6,** 314–320.

Schouten, H., Smith, D.K., Cann, J.R. & Escartín, J., 2010. Tectonic versus magmatic extension in the presence of core complexes at slow-spreading ridges from a visualization of faulted seafloor topography, *Geology,* **38,** 615–618.

Searle, R.C., MacLeod, C.J., Peirce, C. & Reston, T.J., 2019. The Mid-Atlantic Ridge near 13°20′N: high-resolution magnetic and bathymetry imaging, *Geochem., Geophys., Geosys.*, **20,** 295–313.

Serpelloni, E., Vannucci, G., Pondrelli, S., Argnani, A., Casula, G., Anzidei, M., Baldi, P. & Gasperini, P., 2007. Kinematics of the western Africa-Eurasia plate boundary from focal mechanisms and GPS data, *Geophys. J. Int.,* **169**(3), 1180–1200.

Shaw, P.R., 1994. Age variations of oceanic crust Poisson's ratio: inversion and a porosity evolution model, *J. geophys. Res.,* **99**(B2), 3057–3066.

Shearer, P.M., 1988. Cracked media, Poissons ratio and the structure of the upper oceanic-crust, *Geophys. J.,* **92**(2), 357–362.

Shearer, P.M. & Orcutt, J.A., 1986. Compressional and shear-wave anisotropy in the oceanic lithosphere – the Ngendei seismic refraction experiment, *Geophys. J. R. astr. Soc.,* **87**(3), 105–123.

Simão, N.M., Peirce, C., Funnell, M.J., Robinson, A.H., Searle, R.C., MacLeod, C.J. & Reston, T.J., 2020. 3-D P-wave velocity structure of oceanic core complexes at 13°N on the Mid-Atlantic Ridge, *Geophys. J. Int.,* **221**(3), 1555–1579.

Smith, D. & Cann, J., 1990. Hundreds of small volcanoes on the median valley floor of the Mid-Atlantic Ridge at 24–30°N, *Nature,* **348,** 152–155.

Smith, D.K., Cann, J.R. & Escartín, J., 2006. Widespread active detachment faulting and core complex formation near 13°N on the Mid-Atlantic Ridge, *Nature,* **443,** 440–444.

Smith, D.K., Escartín, J., Cannat, M., Tolstoy, M., Fox, C.G., Bohnenstiehl, D. & Bazin, S., 2003. Spatial and temporal distribution of seismicity along the northern Mid-Atlantic Ridge (15°–35°N), *Geophy. Res. Lett.,* **108**(B3), doi:10.1029/2002JB001964.

Smith, D.K., Escartín, J., Schouten, H. & Cann, J.R., 2008. Fault motion and core complex formation: significant processes in seafloor formation at slow-spreading mid-ocean ridges (Mid-Atlantic Ridge, 13°–15°N), *Geochem. Geophys. Geosyst.,* **9**(3), doi:10.1029/2007GC001699.

Smith, D.K., Tolstoy, M., Fox, C.G., Bohnenstiehl, D.R., Matsumoto, H. & Fowler, M., 2002. Hydroacoustic monitoring of seismicity at the slow-spreading Mid-Atlantic Ridge, *Geophys. Res. Lett.,* **29**(11), 13–1-13-4.

Sohn, R.A., Webb, S.C., Hildebrand, J.A. & Cornuelle, B.D., 1997. Three-dimensional tomographic velocity structure of upper crust, coaxial segment, Juan de Fuca Ridge: implications for on-axis evolution and hydrothermal circulation, *J. geophys. Res.,* **102**(B8), 17 679–17 695.

Spudich, P. & Orcutt, J., 1980. Petrology and porosity of an oceanic crustal site: results from wave form modeling of seismic refraction data. *J. geophys. Res.,* **85**(B3), 1409–1433.

Stephen, R.A., Louden, K.E. & Matthews, D.H., 1979. The Oblique Seismic Experiment on DSDP Leg 52, in *Initial Reports of the Deep Sea Drilling Project, 51/52/53,* eds Bryan, W.B. *et al.*, U.S. Government Printing Office, Washington.

Szitkar, F. *et al.*, 2019. Detachment tectonics at Mid-Atlantic Ridge 26°N, *Sci. Rep.,* **9,** 11830.

Tucholke, B.E. & Lin, J., 1994. A geological model for the structure of ridge segments in slow spreading ocean crust, *J. geophys. Res.,* **99,** 11 937–911 958.

Tucholke, B.E., Lin, J. & Kleinrock, M.C., 1998. Megamullions and mullion structure defining oceanic metamorphic core complexes on the Mid-Atlantic Ridge, *J. geophys. Res.,* **103**(B5), 9857–9866.

Wessel, P., Smith, W.H.F., Scharroo, R., Luis, J. & Wobbe, F., 2013. Generic mapping tools: improved version released, *EOS, Trans. Am. geophys. Un.,* **94**(45), 409–410.

White, R.S., Mckenzie, D. & O'Nions, R.K., 1992. Oceanic crustal thickness from seismic measurements and rare earth element inversions, *J. geophys. Res.,* **97,** 683–715.

Wilkens, R.H., Fryer, G.J. & Karsten, J., 1991. Evolution of porosity and seismic structure of upper oceanic crust – importance of aspect ratios, *J. geophys. Res.,* **96**(B11), 17 981–17 995.

Wilson, D.J., Robinson, A.H., Hobbs, R.W., Peirce, C. & Funnell, M.J., 2019. Does intermediate spreading-rate oceanic crust result from episodic transition between magmatic and magma-dominated, faulting-enhanced spreading – the Costs Rica Rift example, *Geophys. J. Int.,* **218,** 1617–1641.

Wilson, S.C., Murton, B.J. & Taylor, R.N., 2013. Mantle composition controls the development of an oceanic core complex, *Geochem. Geophys. Geosyst.,* **14,** 979–995.

Zelt, C.A., 1998. Lateral velocity resolution from three-dimensional seismic refraction data, *Geophys. J. Int.,* **135,** 1101–1112.

Zelt, C.A. & Ellis, R.M., 1988. Practical and efficient ray tracing in two dimensional media for rapid traveltime and amplitude forward modelling, *Can. J. Explor. Geophys.,* **21,** 16–31.

Zelt, C.A. & Barton, P.J., 1998. Three-dimensional seismic refraction tomography: a comparison of two methods applied to data from the Faeroe Basin, *J. geophys. Res.,* **103,** 7187–7210.

Zelt, C.A. & Smith, R.B., 1992. Seismic traveltime inversion for 2-D crustal velocity structure, *Geophys. J. Int.*, **108,** 16–34.

SUPPORTING INFORMATION

Supplementary data are available at *GJI* online.

Figure S1. Slices through the *hit count model* corresponding to the 3-D *S*-wave *inversion model* (Fig. 6) derived using the *sea surface parallel initial model*. Each of the slices represents the number of rays crossing through a model cell as part of the inversion process. See Fig. 6 for details of each slice. An alternative version of this figure based on the 3-D *S*-wave *inversion model* derived using the *seabed following initial model* is provided as Fig. S9.

Figure S2. Slices through the 3-D *S*-wave *inversion model* derived using the *seabed following initial model* (Fig. 5). (a) Bathymetry map showing the proposed spreading centre from Mallows & Searle (2012—blue dashed line), and Simão *et al.* (2020—red dashed line), together with the location of active vent sites (white stars). Black dashed lines in (a) and in all horizontal (depth) slices indicate the locations of the vertical slices through the velocity model. (b) Vertical slice through the *seabed following initial model* (Fig. 5) at $y = 20$ km with the location of the 1320 OCC and its breakaway annotated. (c) Depth slice through the *inversion model* at $z = 4.5$ km bss. (d, f, h and j) Vertical slices through the *S*-wave *inversion model* at the annotated model distances and with relevant features annotated. IFNF—inward-facing normal fault of Simão *et al.* (2020). (e.g. and (i) Depth slices through the *inversion model* at the annotated model depths bss. In all *inversion model* parts, the 3.0 km s^{-1} and 4.5 km s^{-1} *S*-wave velocity contours are annotated, and the slices are masked using the *inversion model* ray coverage. The corresponding hit count, used to demonstrate the ray coverage and define the mask, is provided as Fig. S9. The 4.5 km s^{-1} *S*-wave velocity contour is used as the proxy for the crust-to-mantle transition, based on Simão *et al.* (2020). Depth slices are illuminated by the seabed topography. Model parameters, the number of traveltime picks included in the ray tracing, and the resulting χ^2 and RMS misfit are indicated. An alternative version of this figure based on the 3-D *S*-wave *inversion model* derived using the *sea surface parallel initial model* is provided as Fig. 6.

Figure S3. Slices through the *semblance model* derived from checkerboard testing of the 3-D *S*-wave *inversion model* (Fig. S2) resulting from the *seabed following initial model* (Fig. 5). Each of the slices represents the semblance based on averaging the result of the 32 possible permutations of a 10 × 10 × 2 km checkerboard. The 0.7 semblance contour is used to indicate where model recoverability (resolution) is considered good (Zelt 1998). See Fig. S2 for details of each slice. An alternative version of this figure based on the 3-D *S*-wave *inversion model* derived using the *sea surface parallel initial model* is provided as Fig. 7.

Figure S4. Comparison of the 3-D *S*-wave *inversion model* (Fig. S2), derived using the *seabed following initial model* (Fig. 5), with that of the 2-D transect Profile R (Peirce *et al.* 2020). (a) Bathymetry map showing the proposed spreading centre from Mallows & Searle (2012—blue dashed line), and Simão *et al.* (2020—red dashed line), together with the location of active vent sites (white stars). The location of the profiles shown in (b–e) are indicated by their respective colours. (b) Profile R *S*-wave *inversion model* (Peirce *et al.* 2020), which crosses the southern edge of 3-D grid (*y*-axis = 0 km) at ∼133 km along profile. (c–e) NS trending profiles through the 3-D *S*-wave *inversion model* (Fig. S2), spaced at 2 km intervals ($x = 26$, 28 and 30 km). The model slice at $x = 28$ km (d) is coincident with Profile R (b), although the two show moderately different velocity structures beneath the OCCs. However, the model slice at $x = 30$ km (e) has a closer visual fit, with low *Vs* in the upper crust beneath the OCCs and higher *Vs* in the inter-OCC basin and surrounding area. Vertical slices (b–e) are masked using the ray coverage. See Fig. S2 for details. An alternative version of this figure based on the 3-D *S*-wave *inversion model* derived using the *sea surface parallel initial model* is provided as Fig. 8.

Figure S5. Slices through the *Vp/Vs model* calculated using the *P*-wave *inversion model* (*LRDM*–Simão *et al.* 2020) and the *S*-wave *inversion model* (Fig. S2) derived from the *seabed following initial model* (Fig. 5). (a) Bathymetry map showing the proposed spreading centre from Mallows & Searle (2012—blue dashed line), and Simão *et al.* (2020—red dashed line), together with the location of active vent sites (white stars). Black dashed lines in (a) and in all horizontal (depth) slices indicate the locations of the vertical slices through the velocity model. (b) Vertical slice through the *P*-wave *inversion model* (Simão *et al.* 2020) at $y = 20$ km with the location of the 1320 OCC and its breakaway annotated. The equivalent for the *S*-wave *inversion model* is shown in Fig. S2(d). (c) Depth slice through the *Vp/Vs model* at $z = 4.5$ km bss. (d, f, h and j) Vertical slices through the *Vp/Vs model* at the annotated model distances and with relevant features annotated. (e, g and i) Depth slices through the *Vp/Vs model* at the annotated model depths bss. In all *Vp/Vs model* parts, the 1.85 *Vp/Vs* contour is annotated (Peirce *et al.* 2019b, 2020), and the slices are masked using the *inversion model* ray coverage. See Fig. S2 for details of each slice. An alternative version of this figure based on the 3-D *S*-wave *inversion model* derived using the *sea surface parallel initial model* is provided as Fig. 9.

Figure S6. Slices through the 3-D grid plotted as the difference between the *S*-wave *inversion model* (Fig. S2), derived from the *seabed following initial model* (Fig. 5) and a *reference model*. (a) Bathymetry map showing the proposed spreading centre from Mallows & Searle (2012—blue dashed line), and Simão *et al.* (2020—red dashed line), together with the location of active vent sites (white stars). Black dashed lines in (a) and in all horizontal (depth) slices indicate the locations of the vertical slices through the velocity model. (b) 1-D *P*-wave and *S*-wave *reference model* velocity–depth samples at $x = 42$ km, $y = 30$ km in the corresponding inversion models, location marked by the blue cross in (a), together with the conversion of the *P*-wave sample to *S*-wave using a *Vp/Vs* ratio of 1.7 (black dashed line) for comparison. This location was chosen as Simão *et al.* (2020) interpret it to lie where the crust is currently being formed by magma rich spreading. See text for details of *difference model* construction. (c) Depth slice through the *difference model* at $z = 4.5$ km bss. (d, f, h and j) Vertical slices through the *difference model* at the annotated model distances and with relevant features annotated. (e, g and i) Depth slices through the *difference model* at the annotated model depths bss. In all *difference model* parts, the +0.75 km s^{-1} (equivalent to Simão *et al.*'s 2020 +1.25 km s^{-1} *P*-wave difference contour—e.g. their fig. 7) and +1.25 km s^{-1} contours are annotated, and the slices are masked using the *inversion model* ray coverage. This approach to model representation clearly demonstrates (j) that the 1320 and 1330 OCCs are unlikely to be interconnected features along the same detachment. See Fig. S2 for details of each slice. An alternative version of this figure based on the 3-D *S*-wave *inversion model* derived using the *sea surface parallel initial model* is provided as Fig. 10.

Figure S7. 1320 OCC detachment geometry from slices through the 3-D grid plotted as the difference between the *S*-wave *inversion model* (Fig. S2), derived from the *seabed following initial model* (Fig. 5), and a *reference model* (after Simão *et al.* 2020). a) Bathymetry surrounding the 1320 OCC with microseismic events (Parnell-Turner *et al.* 2017) coloured according to mechanism (see legend). White lines locate cross-sections shown in (b–i) with azimuths or *x*,*y* coordinates annotated in black. White triangle marks the Irinovskoe vent site in all relevant parts and the circled cross the intersection of each cross-section at the OCC (vertical dotted line in all other parts). Red dashed line marks the trend of the proposed spreading centre location based on the crustal structure derived from Simão *et al.*'s (2020) *P*-wave *inversion model*. Mallows & Searle's (2012) average spreading centre is marked by the blue dashed line. Blue cross shows the 1-D reference profile location. (b–i) Vertical cross-sections through the *difference model* at various azimuths, with earthquake hypocentres annotated. Sections are annotated in the top right corners by their azimuths (b–f) or are annotated by their *x* or *y* coordinate (g–i). Red arrows locate Simão *et al.*'s (2020) proposed spreading centre further to the east, based on crustal velocity–depth structure; black arrows indicate the average spreading centre of Mallows & Searle (2012). Red and blue dashed wedges indicate the changing dip (annotated) of the detachment fault plane, based on the +1.25 km s^{-1} velocity difference contour of Simão *et al.*'s (2020) *P*-wave *inversion model*, on the exposed surface and at depth. Horizontal dotted line marks the shallowest depth of the 1320 OCC. IFNF—inward-facing normal fault. In all *difference model* parts, the +0.75 km s^{-1} (equivalent to Simão *et al.*'s 2020 +1.25 km s^{-1} *P*-wave difference contour—e.g. their fig. 7) and +1.25 km s^{-1} contours are annotated. An alternative version of this figure based on the 3-D *S*-wave *inversion model* derived using the *sea surface parallel initial model* is provided as Fig. 12.

Figure S8. 1330 OCC detachment geometry. See Fig. S7 for details. The red circled cross in (a) marks the general location of the non-transform offset (NTO) shown in (e). White triangle marks the Semyenov vent site in all relevant parts. An alternative version of this figure based on the 3-D *S*-wave *inversion model* derived using the *sea surface parallel initial model* is provided as Fig. 13.

Figure S9. Slices through the *hit count model* corresponding to the 3-D *S*-wave *inversion model* (Fig. S2) derived using the *seabed following initial model*. Each of the slices represents the number of rays crossing through a model cell as part of the inversion process. See Fig. S2 for details of each slice. An alternative version of this figure based on the 3-D *S*-wave *inversion model* derived using the *sea surface parallel initial model* is provided as Fig. S1.

Figure S10. Rotating movie 3-D perspective view of the generalized shape of the 1320 and 1330 OCC detachment surfaces based on the +1.25 km s^{-1} contour from Simão *et al.*'s (2020) *P*-wave *difference model*. The location of the reference point (blue cross) and the Semyenov (white star) and Irinovskoe (black star) are shown on the bathymetry plotted above the 3-D view, extended to their seabed depths by the black dashed lines. Black arrow points north.

Figure S11. Rotating movie 3-D perspective view of the generalized shape of the 1320 and 1330 OCC detachment surfaces based on the +0.75 km s^{-1} contour from the *S*-wave *difference model* (Fig. 6) derived using the *sea surface parallel initial model* (Fig. 5). The location of the reference point (blue cross) and the Semyenov (white star) and Irinovskoe (black star) are shown on the bathymetry plotted above each 3-D view, extended to their seabed depths by the black dashed lines. Black arrow points north.